Estudos do Quaternário, 22, APEQ, Braga, 2022, pp. 45-84
https://www.apeq.pt/estudosdoquaternario/index.php/eq

ARCHAEOMETRIC STUDY OF THE PROTO-HISTORIC CERAMICS FROM THE SETTLEMENT OF THE AVECASTA CAVE (FERREIRA DO ZÊZERE, PORTUGAL)

ESTUDO ARQUEOMÉTRICO DA CERÂMICA PROTO-HISTÓRICA DO POVOADO DA GRUTA DE AVECASTA (FERREIRA DO ZÊZERE, PORTUGAL)

ABIODUN O. GANIYU[(1)], MASSIMO BELTRAME[(1,2,4)], JOSÉ ANTÓNIO P. MIRÃO[(1,2,3)], JOSÉ E. MATEUS[(4)]

Abstract:

The Avecasta Cave is the only proto-historic cave recognised as a settlement in the centre of Portugal. Other proto-historic caves in the centre of Portugal were normally used for ritual purposes. Based on its distinct function, it became essential to study uncovered ceramic sherds from the cave to contribute to the history of the people who lived there. So, this research aims to determine the ceramic samples' technology, provenance, physical properties, and changes in the raw materials used to produce ceramics, with a chronology comprised between the Neolithic and the Iron Age. Optical Microscope, X-ray Diffraction, X-ray Fluorescence, Scanning Electron Microscope coupled to Energy Dispersive Spectrometer, and a Helium Gas Pycnometer were used to accomplish these goals. The results of the analysed samples reveal four groups of different mineralogical and chemical composition, and establish their probable provenance and physical properties.

Keywords: Avecasta Cave, Proto-Historic Ceramic, Ceramic technology, Provenance, Archaeometry

Resumo:

A Gruta de Avecasta é a única gruta proto-histórica identificada como povoado na área central de Portugal. Outras grutas proto-históricas na mesma região foram utilizadas apenas para fins rituais. Pela sua função distinta, tornou-se imprescindível o estudo dos fragmentos cerâmicos encontrados na gruta, contribuindo para o conhecimento das sociedades que ocuparam o espaço. Este trabalho visa determinar a tecnologia usada, proveniência, propriedades físicas e possíveis mudanças de matérias-primas cerâmicas usadas do Neolítico à Idade do Ferro. Petrografia de cerâmicas, Difração de Raios-X, Fluorescência de Raios-X, Microscópio Eletrónico de varrimento acoplado a Espectrómetro de Dispersão em Energia, além dum Picnómetro de Gás Hélio foram utilizados para atingir estes objetivos. Os resultados do estudo revelam quatro grupos, com diferentes composições mineralógicas e químicas, estabelecem a sua possível proveniência e identificam as suas propriedades físicas.

Palavras-chave: Gruta de Avecasta, Cerâmica Proto-Histórica, Tecnologia cerâmica, Proveniência, Arqueométria

Received: 15th November, 2022; Accepted: 8th December, 2022

1. INTRODUCTION

The study of material cultures from prehistoric caves in Portugal dates back to the 19th century (OOSTERBEEK 1993). Nery Delgado was the first who write about the significance of the cave to the early Man during the middle Palaeolithic and the late Neolithic periods, when he uncovered significant findings at the Furninha Cave on the southern slopes of the Peniche peninsula (DELGADO 1884). Other scholars such as Pedro Bosh-Gimpera and Navarrete Enciso studied the decorations on pottery sherds from different caves in the centre of Portugal. Ceramics were associated to four typical cultures - *Cardium* ulture, Beaker culture, Los Millares culture, and Phoenicians culture - in Iberia (NAVARRETE & ENCISO 1976). Subsequent studies, carried out on ancient pottery assemblages excavated from different caves in the centre of Portugal, gave indication on the ancient caves function. Gruta de Caldeirão, for instance, underwent archaeological excavation between 1979 and 1988. The lack of archaeobotanical remains (i.e. cereals grains) and the typological study of archaeological pottery suggested that the site was mainly utilized for funerary purposes and/or rituals (ZILHÃO 1988). Other caves in the centre of Portugal, whose pottery assemblages were interpreted to have had the same function include Gruta do Cadaval, Gruta dos Ossos, and Gruta do Morgado (OOSTERBEEK 1993).

Among a few caves in the Centre of Portugal whose functions differ from funerary practice is the Avecasta Cave in the municipality of Ferriera do Zêzere. The Cave functioned as a domestic dwelling, rural stocking and artisanal nucleus, and it housed ancient people from the Neolithic to the Middle Ages. This was revealed by the material culture uncovered from well-documented archaeological layers of the site (MATEUS & QUEIROZ 2012). Thus, the Cave can be considered one of the

(1)HERCULES Laboratory, University of Évora, Largo Marquês de Marialva nº 8, 7000-809, Évora, Portugal
(2)Associated Laboratory In2Past
(3)Department of Geosciences, University of Évora, Rua Romão Ramalho, nº 59, 7000-671 Évora, Portugal
(4)Double U (W) Replay, 2560-309, Torres Vedras, Portugal, Corresponding author: Massimo Beltrame (massimo@uevora.pt)

longest and best-preserved stratigraphic sequence of "old" cultures and habitats in Portugal during the proto history (MATEUS & QUEIROZ 2012).

Archaeometric studies of pottery in the centre of Portugal are also rare. William K. Barnett was the first researcher who carried out these kinds of studies. He characterizes Early Neolithic ceramics from the Gruta do Caldeirão (BARNETT 1987). His research focused on the technological characterization and on provenance of Early Neolithic ceramic. Another archaeometrical study has been developed on a limited number of ceramic fragments (i.e. from the Bronze Age) recovered in an archaeological site close to the Avecasta Cave (BELTRAME *et al.* 2019), but the archaeological context was different.

This work will focus on the archaeometric of ceramics recovered at the Avecasta Cave (Ferreira do Zêzere, Portugal). Differently from previous studies, the main goal of this research will be the evaluation of ceramics characteristics, technology, and provenance. Samples chronology is comprised between the Late Neolithic and the Iron age. So, it will also be possible to evaluate the continuity of raw material/s exploitation for ceramic production during different periods, adding new information to the few archaeometric studies developed on proto-historic ceramics from the centre of Portugal.

To reach these goals, this research will employ a multi-analytical approach, including optical microscopy (OM), mineralogical analysis by powder X-ray Diffraction (XRD), chemical analysis by X-Ray Fluorescence (XRF), and microstructural analysis by a Scanning Electron Microscope coupled to Energy Dispersive Spectrometer (SEM-EDS). Porosity (open and close) will also be evaluated using a Helium gas pycnometer.

2. THE ARCHAEOLOGICAL SITE

2.1. Geographical Location of the Avecasta Cave

Avecasta is a small village situated in the centre of Portugal (Fig. 1) in the Ferreira do Zêzere municipality. Its geographical coordinates are 39° 45'00.0" North and 8°24'00.0" West, and it covers 0.9812 km^2 land area. It is located at an elevation of 216 meters above sea level, and its UTM position is NE50. Its Joint Operation Graphic reference is NJ29-02. Avecasta is about 24 km farther from Tomar to the North, and about 62 km distant from Coimbra to Avecasta to the South. The Cave of Avecasta is situated to the north-west of the Avecasta village, which gives it its name.

The Cave (Fig. 2), which continuously housed ancient people from the Neolithic up to the end of the Middle Ages, is about 60 meters in diameter in its modern emergent physiognomy (MATEUS & QUEIROZ 2012). Its original shape might be a large ovoid void filled with local sediments and by the partial collapse of the Cave roof (MATEUS & QUEIROZ 2012), allowing cryoclastic periglacial deposits to accumulate. However, without these deposits, the Cave was assumed to be an ample hollow space shaped like an ellipsoid of revolution. The antique Cave was once fenced with a system of walls, but this (partly collapsed ruin) remains yet to be excavated (MATEUS & QUEIROZ 2012).

Fig. 1. Map of the Iberian Peninsula showing the location of the Avecasta Cave.
Fig. 1. Mapa da Península Ibérica com localização da Gruta de Avecasta.

Fig. 2. Frontal view of the gate of the Avecasta Cave.
Fig. 2. Imagem frontal da entrada da Gruta de Avecasta.

2.2. Archaeological Context

In the last four decades, precisely between 1980 and 2017, the cave witnessed a series of excavation campaigns that uncovered traces of several dwellings. Artisanal and protecting structures of diverse periods, such as stone walls and palisades (induced by post-holes) stone pavements, fireplaces, and metallurgic pit forges (Mateus & Queiroz 2012) were excavated. The major digging sector is six metres large (3x3m) and 7 meters deep (Fig. 3) and provided the primary extended stratigraphical profile of the site (Mateus & Queiroz 2012). Due to the excellent preservation of the stratigraphical matrix several ancient remains, including ceramic fragments, stone tools, metal works, bones, and plant remains have been collected and allow detailed analytical enquiry (Mateus & Queiroz 2012). The radiocarbon dating (AMS) of charcoal fragments and seed chards from seven out of the whole layers permitted indirect dating of uncovered artifacts, including ceramic (Mateus & Queiroz 2012).

2.3. Geological Context

The local geology of the archaeological site of Avecasta is complex (Fig. 4). The site's geological complexity occurs due to the closeness with different tectonostratigraphic terranes and the high deformation area of Porto-Tomar Shear Zone (PTSZ). The cave is located in the Lusitanian Meso -Cenozoic Basin (LB) and is composed mainly of sedimentary rocks (Manuppella *et al.* 2000). However, considering a10 to 15 km radius from the site, it also shares boundaries with the Central Iberian Zone (CIZ) and the Porto-Tomar Shear Zone (PTSZ) (Azerêdo 2007). Each of these zones has different lithologies, and thus contributed to the geological diversity of the Avecasta archaeological area.

Moving eastward, considering a 10 to 15 km radius from the cave, the Lusitanian Basin encloses Lower Jurassic limestones, dolostones, and marls outcrops (i.e., A7 in Fig. 4), interrupted by a Triassic-Jurassic sandstone formation included in the *Silves* group (i.e. *Grés de Silves* – A8 in Fig. 4) (Soares *et al.* 2007). However, moving further eastward, outcrops of the PTSZ/CIZ geological zone can be found. They are characterised by medium to high and medium to low grade metamorphic units, which are attributed to Neoprotetrozoic formed by orthogneisses, paragneisses, micaschists, slates, and metagreywackes (Moreira *et al.* 2016; Romão 2006). Part of the CIZ zone also comprises geological formations from Phanerozoic (Paleozoic-Ordovician/Cambrian) with rock types ranging from plutonic granite-orthogneiss to schist, sandstone, quartzite, and conglomerate (Romão 2006).

Moving westward, considering 10 to 15 km radius from the site, the Lusitania Basin is mainly characterised by Middle Jurassic limestone, dolostone of different textures, sometimes with oolites (Manuppella *et al.* 2000) (i.e., A6 in Fig. 4). Still heading westward, the geology of the area is also characterised by the presence of upper Jurassic, marly limestones, and fine-grained sandstones (i.e., A5 in Fig. 4). It also encloses Lower Cretaceous limestones, dolostones, and sandstones (i.e., A4 &A3 in Fig. 4) together with Neogene or Miocene clay deposits (i.e., A2 in Fig. 4) (Teixeira *et al.* 1968), and quaternary alluvial deposits (i.e., A1 in Fig. 4).

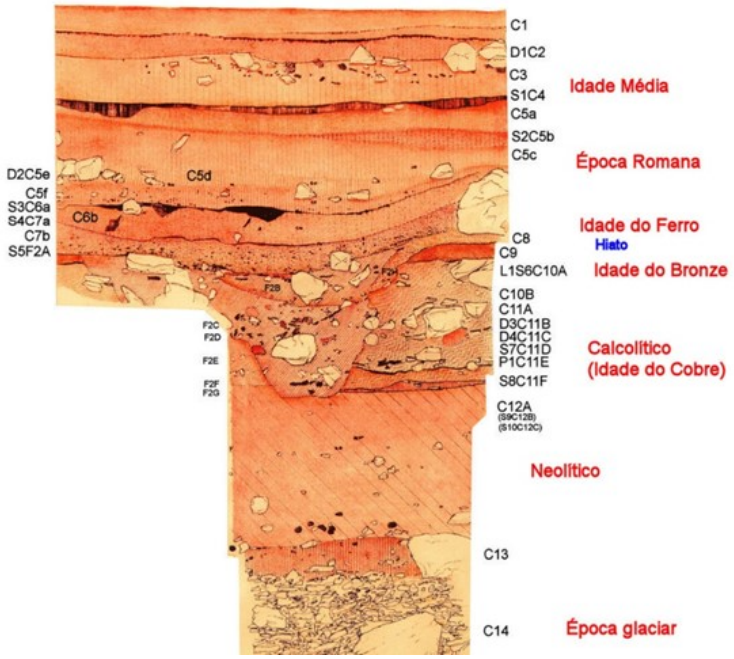

Fig. 3. Stratigraphic profile of the excavated area (Mateus & Queiroz 2012). Profile height: 4,5 m.
Fig. 3. Corte estratigráfico da área escavada (Mateus & Queiroz 2012). Altura do corte: 4,5 m.

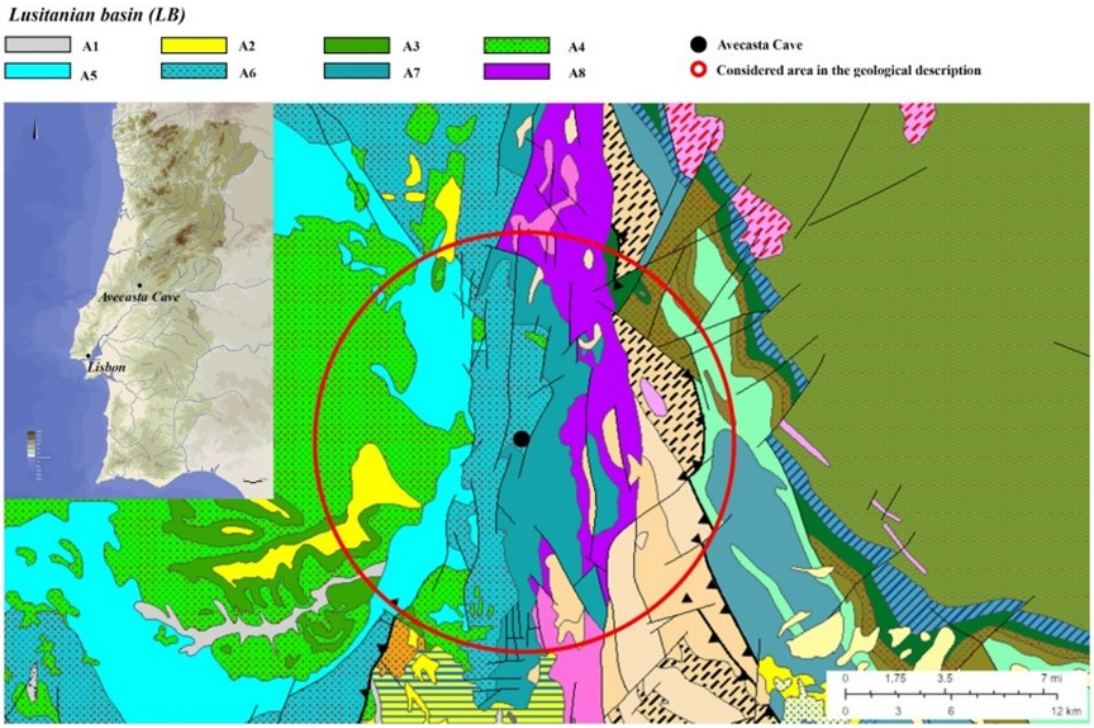

Fig. 4. Geological map of the Avecasta Cave area (https://geoportal.lneg.pt/mapa/#).
Fig. 4. Mapa geológica da área da Gruta de Avecasta (https://geoportal.lneg.pt/mapa/#).

3. CERAMIC MATERIALS

Selected samples are forty-two (42) in total, and the relative chronology spans between the Late Neolithic and the Iron Age (Table 1). Ceramics are highly fragmented. It was, therefore, not possible/easy to understand vessel shapes. Hence, this work will not attempt to link results with ceramics typology. Nevertheless, some observations were possible in some cases, and fragments of bowls and vases could be observed. The bowl shapes identified are sub-spheric bowls, big hemispheric bowls, small hemispheric bowls, and carinated bowls. The vase types recognised are small and big vases. Some rims and wall pieces of uni-

dentified shapes were also selected. The observed shapes have some similarities with pottery sherds described by STOJANOVSKI *et al.*, excavated from Anta 1 de Val da Laje passage grave, about 20 kilometres from the Avecasta cave. In this case ceramic chronology spans between the Neolithic and the Chalcolithic period (STOJANOVSKI *et al.* 2020). However, STOJANOVSKI *et al.* in addition to bowl and vases also recognised another set of ceramic types and shapes. Amongst them jars, globular pots, and some bowls of trunco-conic shapes were observed, and they were never recognised in the visual observation of our forty-two samples selected for this study. Regarding the sherds' sizes, all the samples are between 3 cm and 10 cm in diameter. In some cases, the surfaces of the ceramic fragments appear rough, in other case, several fragments exhibit simple surface treatments of slips applications and burnished surfaces.

Regarding ceramic sampling (Table 1), the following number of sherds were selected from different archaeological layers:
- Four (4) samples layer C9, Iron Age;
- Eleven (11) samples in total from layers C9/C10, C10A and C11B, Bronze Age;
- Twenty-two (22) samples in total from layers C11C to C11F, Chalcolithic period;
- Five (5) ceramic fragments in total from layers C12 and C12/13, Late Neolithic.

However, only three archaeological layers (i.e. C10A, C11C, and C11E) were dated by radiocarbon dating of charcoal fragments using Accelerated Mass Spectrometry (AMS) equipment (José Matheus personal communication). The chronology of these layers archaeological can be included between the local Middle Chalcolithic (layer C11E), Late Chalcolithic (layer C11C), and the Bronze Age (layer C10A).

Table 1. Serial number, chronology, archaeological layer, reference number, and description of the analysed ceramic samples.
Tabela 1. Número serial, cronologia, nível arqueológico, número de referência, e descrição das amostras de cerâmica analisadas.

Serial Number	Provisional Chronology	Arch. Layer	Group	Reference No.	Description
AVE_S1	Iron Age	C9	Group 42	AVE P28-211	Wall Fragment with burnished surface
AVE_S2	Iron Age	C9	Group 42	AVE P28-166	Wall Fragment with a burnished surface
AVE_S3	Iron Age	C9	Group 42	AVE R27-90	Wall frag. With a burnished surface
AVE_S4	Iron Age	C9	Group 41	AVE R27-87	Vase with slip
AVE_S5	Late Bronze Age	C9/C10	Group 43	AVE R28-528	Small Vase with slip
AVE_S6	Late Bronze Age	C9/C10	Group 43	AVE R28-512	Small Vase with slip
AVE_S7	Mid Bronze Age	C10A	Group 27	AVE R27-465	Big Vase with burnished surface
AVE_S8	Mid Bronze Age	C10A	Group 27	AVE P28-168	Big vase with burnished surface
AVE_S9	Mid Bronze Age	C10A	Group 28	AVE R27-462	Big Vase with burnished surface
AVE_S10	Mid Bronze Age	C10B	Group 40	AVE R27-478	Vase with slip
AVE_S11	Mid Bronze Age	C10B	Group 40	AVE R27-463	Big Vase with slip
AVE_S12	Early Bronze Age	C11A	Group 25	AVE R27-601	Carinated Bowl with a burnished surface
AVE_S13	Early Bronze Age	C11B	Group 29	AVE R28-540	Small Vase with slip

Table 1. Serial number, chronology, archaeological layer, reference number, and description of the analysed ceramic samples (cont).
Tabela 1. Número serial, cronologia, nível arqueológico, número de referência, e descrição das amostras de cerâmica analisadas (cont).

Serial Number	Provisional Chronology	Arch. Layer	Group	Reference No.	Description
AVE_S14	Early Bronze Age	C11B	Group 29	AVE P27-604	Vase with handle finished with a slip
AVE_S15	Early Bronze Age	C11B	Group 29	AVE Q28-579	Wall Fragment with burnished surface
AVE_S16	Late Chalcolithic	C11C	Group 15	AVE R28-609	Vase finished with slip
AVE_S17	Late Chalcolithic	C11C	Group 14	AVE Q28-567	Wall Carinated Vase with slip
AVE_S18	Late Chalcolithic	C11C	Group 14	AVE R28-570	Hemispherical Bowl with slip
AVE_S19	Late Chalcolithic	C11C	Group 14	AVE R27-507	Small Bowl with a slip
AVE_S20	Late Chalcolithic	C11C	Group 14	AVE P28-526	Wall frag. Finished with a slip
AVE_S21	Late Chalcolithic	C11C	Group 13	AVE Q28-553	Rim with slip
AVE_S22	Late Chalcolithic	C11C	Group 12	AVE Q28-606	Carinated Pot with slip
AVE_S23	Late Chalcolithic	C11C	Group 12	AVE R27-510	Slimy and Spherical Bowl with a burnish surface
AVE_S24	Late Chalcolithic	C11D	Group 19	AVE R27-581	Small Bowl with a burnished surface
AVE_S25	Late Chalcolithic	C11D	Group 32	AVE P28-578	Hemispheric Bowl with a burnished surface
AVE_S26	Late Chalcolithic	C11D	Group 21	AVE R28-604	Sub-spheric Bowl with slip
AVE_S27	Mid-Chalcolithic	C11E	Group 4	P28-620	Small Hemispheric Bowl with burnished surface
AVE_S28	Mid-Chalcolithic	C11E	Group 3	AVE P28-703	Small Vase
AVE_S29	Mid-Chalcolithic	C11E	Group 3	AVE P28-623	Small Hemispheric Bowl with slip
AVE_S30	Mid-Chalcolithic	C11E	Group 1	AVE Q28-727	Hemispheric Bowl
AVE_S31	Mid-Chalcolithic	C11E	Group 1	AVE Q28-726	Hemispheric Bowl with burnished surface

Table 1. Serial number, chronology, archaeological layer, reference number, and description of the analysed ceramic samples (cont).
Tabela 1. Número serial, cronologia, nível arqueológico, número de referência, e descrição das amostras de cerâmica analisadas (cont).

Serial Number	Provisional Chronology	Arch. Layer	Group	Reference No.	Description
AVE_S32	Mid-Chalcolithic	C11E	Group 1	AVE Q28-713	Hemispheric Bowl with slip
AVE_S33	Early Chalcolithic	C11F	Group 7	AVE R28-850	Wall fragment with burnished surface
AVE_S34	Early Chalcolithic	C11F	Group 7	AVE P28-806	Small Hemispher-ic Bowl with burnished surface
AVE_S35	Early Chalcolithic	C11F	Group 5	AVE Q28-877	Wall Frag.
AVE_S36	Early Chalcolithic	C11F	Group 5	AVE R28-825	Hemispheric Bowl with bur-nished surface
AVE_S37	Early Chalcolithic	C11F	Group 5	AVE P28-780	Carinated Vase with burnished surface
AVE_S38	Transition from Neolithic to chal-colithic period	C12	Group 26	AVE Q27-156	Wall fragment painted with burnished surface
AVE_S39	Transition from Neolithic to chal-colithic period	C12	Group 26	AVE P27-161	Wall fragment painted with burnished surface
AVE_S40	Neolithic	C12B	Group 33	AVE P27-106	Wall fragment finished with slip
AVE_S41	Neolithic	C12/13	Group 35	AVE P27-201	Wall frag. coated with slip
AVE_S42	Neolithic	C13	Group 34	AVE R27-207	Wall fragment painted with slip

4. METHODS

Samples were analysed by Optical Microscope (OM), X-ray Fluorescence (XRF), X-Ray Diffraction (XRD), Scanning Electron Microscope coupled to Energy Dispersive Spectrometer (SEM-EDS). Helium gas Pycnometer was used to determine the physical properties of the samples.

4.1. Optical Microscopy (OM)

Thirty micra thick thin-sections were first prepared. A modified description scheme proposed by (Quinn, 2013) was used to characterize the 'ceramic thin sections, and the textural analysis, including grain size distribution. The estimations of 2D distribution of the different granulometric classes and temper percentages, were obtained using ImageJ software 1.51k (Sitzia *et al.* 2022), which acquired the images obtained under crossed Nicols (XPL) and converted them into binary images. The microscope used for the ceramic thin section analysis was a transmitted light petrographic microscope, model Leica DM-2500-P, equipped with an acquisition camera model Leica MC-170-HD. The HRX-01 HIROX Microscope, equipped with a 5 MP sensor and HR-5000E lens at 0º inclination, were used to acquire high resolution images of samples at 140x magnifications.

4.2. X-Ray Diffraction (XRD)

XRD analyses were developed on powdered samples. The equipment utilized was Bruker AXS

D8 Discover with the Da Vinci design, using a Cu Kα source operating at 40 kV and 40 mA and a Lynxeye 1-dimensional. The scans ran on each sample ranged from 3 to 75 º 2θ, with 0.05 2θ step and 1s/step measuring time by point. A Soler slit and slit of 0.6 mm were applied to the X-ray beam. The interpretation of XRD patterns was performed using Diffract-EVA software with a PDF-2 mineralogical database (International Centre for Diffraction Data - ICDD).

4.3. X-ray Fluorescence (XRF)

X-ray fluorescence (XRF) was applied for all ceramic samples, concretely for the quantification of major oxides (SiO_2, TiO_2, Al_2O_3, Na_2O, K_2O, CaO, MgO, MnO, FeO, P_2O_5), and some minor elements (Rb, Sr, Y, Zr, Nb, Ba, Th, Cr, Co, Ni, Cu, Zn, Ga, As, Pb, V, U, Mn). Analyses were performed with an S2 Puma (Bruker) energy-dispersive X-ray spectrometer (BELTRAME *et al.* 2019; BELTRAME *et al.* 2021). A description of the standard reference materials (SRM) utilised in the calibration method can be found elsewhere (BELTRAME *et al.* 2019). Samples were fused in a Claisse LeNeo heating chamber, using a flux (Li–tetraborate) to prepare fused beads (ratio sample/flux = 1/10). The software utilised for data acquisition and processing was Spectra Elements 2.0, which reported the final oxide/element concentrations and the instrumental statistical error (Stat. error) associated with the measurement. The loss on ignition (LOI) evaluation was carried out by calcination. Roughly 1g of each dry sample was put in a crucible and then placed in a muffle furnace for 1 hour at 1050 °C.

4.4. Scanning Electron Microscope coupled to Energy Dispersive Spectrometer (SEM-EDS)

The ceramic pastes were characterized using a variable pressure HITACHI S3700N SEM coupled with a Quantax EDS microanalysis system. The Quantax system was equipped with a Bruker AXS XFlash® Silicon Drift Detector (129 eV Spectral Resolution at FWHM/MnKα). Standardless PB/ZAF quantitative elemental analysis was performed using the Bruker ESPRIT software. The operating conditions for EDS analysis were as follows: backscattering mode (BSEM), 20 kV accelerating voltage, 10 mm working distance, 120 μA emission current, and 40Pa pressure in the chamber. The detection limits for major elements with atomic mass above sodium were in the order of 0.1wt%. The instrumental statistical uncertainty was 1σ.

4.5. Helium gas Pycnometry

To perform Helium pycnometry tests (i.e. to evaluate ceramic samples physical properties) a micrometric ACCUPYCII 1345 helium gas pycnometer with a 10cc cell volume was used. All the ceramic subsamples of roughly 1x1x1 cm were utilized. The full methodology adopted to evaluate physical properties can be found elsewhere (BELTRAME *et al.* 2020).

5. RESULTS AND DISCUSSION

5.1. Optical Microscopy (OM)

Ceramic optical microscopy results (see annexed file for individual sample characteristics) indicated the presence of four different fabrics. The analysis allowed the observation of each fabric's features, including ceramic matrix, temper, and porosity characteristics (i.e. shape and size). Moreover, image analysis made possible the estimation of temper concentration and grain size distribution. OM was also important to understand the raw materials used in ceramic production, to evaluate the continuity/discontinuity in raw material exploitation, to suggest possible raw material sources, and to evaluate locally and non-locally produced artifacts.

Fabric 1 – Primary calcite rich.

Fabric 1 includes 17 ceramic samples (Fig. 5A). The ceramic paste is generally brown, iron-rich, and slightly homogenous. Porosity is composed of vesicles, elongated voids, and vughs of different sizes. Temper abundance is included between 17.13 and 28.81%, and the maximum grain size is 3.4 mm. Regarding temper morphology, equant grains are dominant, and rarely elongated ones have been observed. Roundness varies from angular to sub-rounded, but angular grains are very abundant. Grain size distribution is mainly unimodal (i.e., the sandy fraction is dominant), and just in some cases bimodal (i.e., the silty fraction is less represented than the sandy ones). Sorting and alignment are poor. From the mineralogical point of view, big primary angular calcite crystals included in the sandy fractions are dominant. In several cases, the firing process thermally altered calcite crystals, and they might look fractured. Quartz, feldspars, and muscovite could also be present, but they are included in the silty fraction. Amongst rock fragments, limestone, quartzite, and marbles (?) were also observed.

Fabric 2 – Quartz - Biotite rich.

Fabric 2 includes 10 ceramic samples (Fig. 5B and 5C). The ceramic paste is brown/dark brown, iron-rich, and moderately homogeneous. Porosity is comprised of vesicles, elongated voids, and vughs of different sizes. Temper concentration is heterogeneous, and it ranges between 4.73% and 27.80%, and maximum grain size is 5.48 mm. Elongated grains were observed, but equant grains appear to be slightly more abundant. Roundness varies from sub-angular to rounded. Grain size distribution is bimodal (i.e., the silty fraction is more abundant than the sandy one) and, in some cases, unimodal (with more silty grains) distribution could be observed. Alignment is poor; sorting is poor to moderate. From a mineralogical point of view, quartz and biotite are dominant. Feldspars (i.e., plagioclase feldspars seem to be more abundant than potassium-rich feldspars), muscovite, and white amphibole (i.e. less represented) have also been observed. Regarding rock fragments, granitic rocks, schists (rich in biotite), and quartzite were

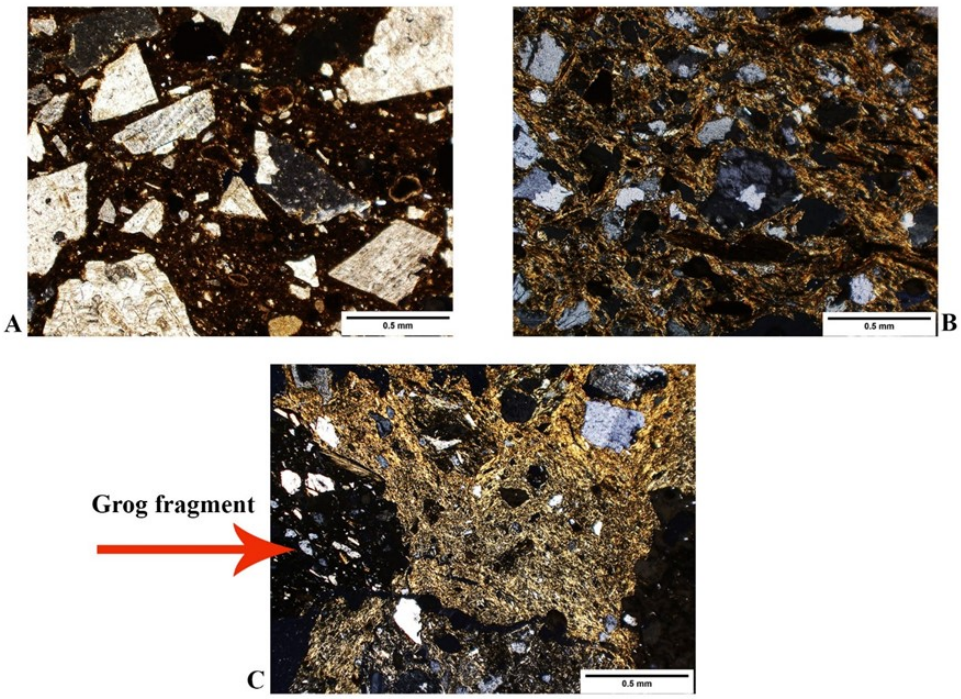

Fig. 5. Pictures of fabrics 1 and 2, collected at 140X magnification. A) Sample Ave R28-850 representing fabric 1; B) Sample Ave R27-465 representing fabric 2; C) Sample Ave R28-609 representing of fabric 2 sample with grogs.
Fig. 5. Imagens do fabrico 1 e 2, obtidas com uma magnificação de 140X. A) Amostra Ave R28-850 do fabrico número 1; B) Amostra Ave R27-465 do fabrico número 2; C) Amostra Ave R28-609 do fabrico número 2 com fragmentos de grog.

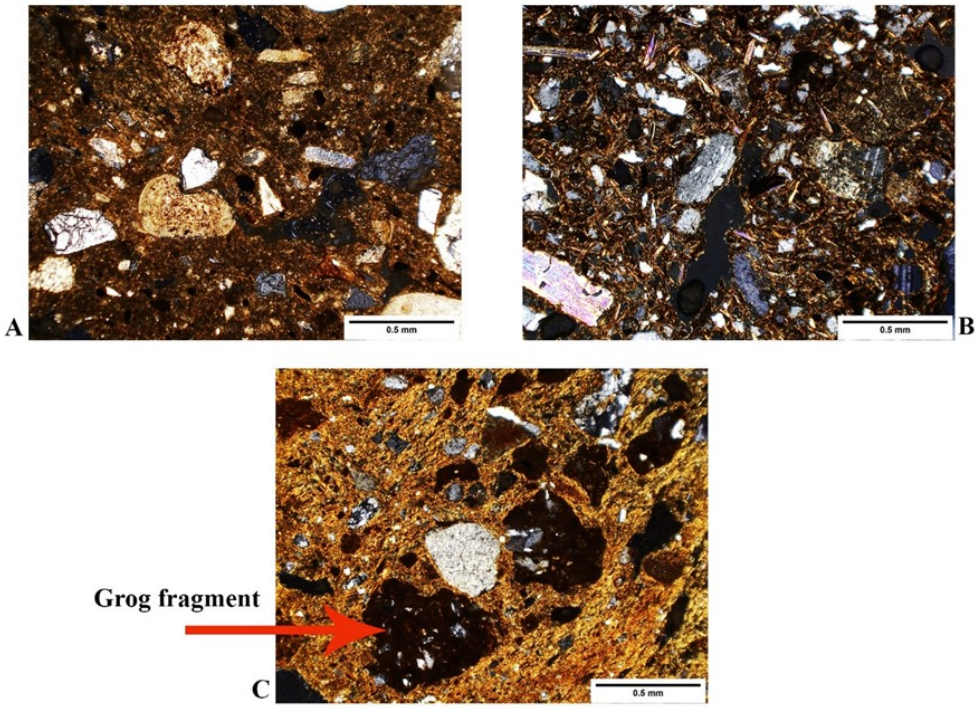

Fig. 6. Representative micrographs of fabrics 3 and 4, collected at 140X magnification. A) Sample Ave Q28-877 representing fabric 3; B) Sample Ave P28-620 representing fabric 4; C) Sample Ave P27-201 representing fabric 4 with grog fragments.
Fig. 6. Imagens do fabrico 3 e 4, obtidas com uma magnificação de 140X. A) Amostra Ave Q28-877 do fabrico número 3; B) Amostra Ave P28-620 do fabrico número 4; C) Amostra Ave P27-201 do fabrico número 4 com fragmentos de grog.

observed. Moreover, some samples (three in total) included in this fabric present grog fragments (Fig. 5C). Grog mineralogical composition is very similar to the mineralogy of the fabric.

Fabric 3 – Quartz – Limestone fragments rich.

Fabric 3 comprises 7 ceramic samples in total (Fig. 6A). The ceramic paste is brown in colour, iron-rich, and slightly heterogeneous. Porosity is comprised of vesicles, elongated voids, and vughs of variable sizes. Temper abundance is included between 7.83 and 24.07%, and the maximum grain size is 3.6 mm. Regarding temper morphology, equant grains are dominant, and rarely elongated ones have also been observed. Roundness varies from sub-angular to rounded. Grain size distribution varies from bimodal to unimodal. Sorting and alignment are poor. From the mineralogical point of view quartz, feldspars, and muscovite have been observed. Among the rock fragments, limestones fragments are very abundant but, quartzites, sandstones, and calcarenite fragments (i.e. in the sample Q28-877) could also be observed.

Fabric 4 – **Quartz-Muscovite rich.**

Fabric 4 includes 8 ceramic samples (Fig. 6B and 6C). The ceramic paste is brown, iron-rich, and moderately homogeneous. Porosity is composed of vesicles, elongated voids, and vughs of variable sizes. Temper concentration ranges between 7.51% and 25.30%, and maximum grain size is 2.22 mm. In terms of temper morphology equant grains look dominant, but elongated ones are well represented in the silty fraction. Roundness varies from sub-angular to rounded. Grain size distribution is bimodal. Sorting and alignment are poor. Mineralogically speaking quartz and muscovite are dominant. Potassium-rich feldspars and plagioclase feldspars were also observed. Amphiboles were very rare or absent. Amongst rock fragments granitic rocks, schists (muscovite rich), and quartzites were identified. Additionally, some samples (four in total) included in this fabric present grog fragments (Fig. 6C). Grog mineralogical composition is very similar to the mineralogy of the fabric.

The results obtained during petrographic analysis point to a difference in the raw materials used to produce each fabric. Results also indicated disparities in part of the manufacturing processes. Regarding fabric 2 and 4 mineralogical composition, they are clearly different. In the first case biotite is an important mineralogical phase (i.e. fabric 2) while, in the second case, muscovite minerals area clearly more represented (i.e. fabric 4). In terms of the manufacturing process, both fabrics, also show some distinctions.

Fabric 2 presents well to moderately sorted temper grains with a slightly heterogeneous matrix, implying that the potters carefully treated the additives used to produce this fabric but channelled lesser efforts towards ensuring adequate clay mixing (Beltrame *et al.* 2020). Fabric 4 on the other hand, has poorly sorted tempers with a moderately homogeneous matrix meaning less temper treatment and sufficient clay mixing (Beltrame *et al.* 2020) by the potter.

Similarly, fabrics 1 and 3 show clear disparities in temper composition. Both contain limestone inclusions, but limestone fragments are much more abundant in fabric 3 than in fabric 1. Aside from this, quartz inclusions in fabric 3 are more abundant than that of fabric 1 ceramic samples. In addition, in fabric 1 calcite crystals are very angular, so calcite rich rock fragments were crushed and added to the ceramic paste. On the contrary, in the case of fabric 3, rounded fragments of limestone and quartz were used. This implies no voluntary milling and, probably, they were included in the sediment used to produce these ceramics. Moreover, the presence of abundant big calcite crystals in fabric 1, and limestones fragments in fabric 3 ceramic samples implies that the potters, perhaps, fired these ceramics at a temperature between 700^{o} C and 800^{o} C (Fabbri *et al.* 2014), Besides, they are both present, and they have not been absorbed in the ceramic paste. This observation cannot be considered conclusive, and more data will be presented in the following sections.

Fig. 7. A rock fragment inside the cave with recrystallized calcite crystals(left), and the result of limestone dissolution (right) in the cave floor.
Fig. 7. Um fragmento rocha no interior da gruta com cristais de calcite recristalizada (esquerda), e o resultado da dissolução do calcário no chão da gruta.

Table 2. Number of included in each fabric for different chronological periods.
Tabela 2. Número de amostras incluídas em cada fabrico por cada período cronológico.

Distribution of samples within each fabric for different chronological periods				
Fabric	Iron Age	Bronze Age	Chalcolithic	Neolithic
1	1	3	13	0
2	2	5	3	0
3	1	2	2	2
4	0	1	4	3
Total	4	11	22	5

To summarize, the raw materials employed to produce each fabric were different, and some of their production processes were also not the same.

Result also provides a clue on the origin of the tempering materials used to produce ceramic samples. Fabric 3 tempers match with the sedimentary rocks of the Lusitanian Meso-Cenozoic Basin where the cave lies. In the case of fabric 1, the addition of big calcite crystals to the ceramic paste might raise doubt regarding its provenance. The identification of many fragments of polycrystalline calcite (i.e., initially classified as marble fragments) must be clarified, as marble outcrops are not common close to the archaeological site. So, to buttress this argument, during ceramic sampling, an inspection of the cave was performed with archaeologists. Limestone dissolution, followed by recrystallization was noted in several points of the cave. Moreover, big calcite crystals could be identified inside the cave if the rock fragment (i.e. probably speleothems fragments originally) was broken (Fig. 7). This means that, in the past, potters from the cave could obtain calcite as tempering material (they could be identified this material easily), and to add it could be added to the ceramic paste to mitigate ceramic paste volume loss during firing.

Limestone dissolution phenomena, and the speleothems formation inside caves have been extensively discussed by Perrin *et al* and Veizer (Veizer 1978; Perrin *et al.* 2014). So, a ceramic production inside the cave can be assumed in the case of fabric 1 samples.

In the case of fabric 2 and 4, temper characteristics clearly indicate similarities with the outcrops of the PTSZ/CIZ zones, which lie 10 to 15 km from the cave. In any case, the predominant mineralogical assemblage of fabric 2 and 4, also suggest the exploitation of different raw materials to produce ceramics.

Lastly, the petrographic analysis suggests a change in the raw materials used for ceramic production across the chronological scope of this work (Table 2). Although the number of samples is not equally distributed amongst the different periods, these observations can give useful indication to develop future studies. In the Iron Age, potters used all the fabrics for ceramic production except for fabric 4. The cessation of the use of fabric 4 for ceramic production in the Iron Age indicates a discontinuity in ceramic sample production technology. The discontinuity was more apparent in the Neolithic period because potters did not utilize fabric 1 and fabric 2 materials for ceramic production during that time. The non-utilization of some fabrics at a particular period within the chronological scope of our research suggests a discontinuity in the raw materials employed for ceramic production.

5.2. X-ray Diffraction (XRD)

X-ray diffraction results (Table 3) complements the OM observation. The mineralogical phases identified include quartz, calcite, illite-muscovite, kaolinite, feldspar (i.e., including K-rich and plagioclase feldspars), dolomite, biotite, amphibole, talc, goethite, halite, anatase, and hematite (Table 4)). The observation of different dominant/major mineralogical phases, also in this case, permit samples subdivision into four major XRD groups.

XRD Group 1. It corresponds to fabric 1 samples. Calcite (very abundant) appears as the dominant mineralogical phase in all cases. Less represented mineralogical phases are quartz (scarce to traces) and illite-muscovite (scarce to traces). Dolomite, hematite, and halite were not identified in all samples.

XRD Group 2. It corresponds to fabric 2 after OM observations. In this group, quartz (very abundant) is the predominant mineralogical phase. Less represented minerals are biotite (scarce), illite-muscovite (moderate), potassium feldspar (scarce to moderate), and plagioclase (scarce to moderate). Amphibole (scarce to moderate), kaolinite (moderate to scarce), talc (moderate), goethite (scarce), and hematite (scarce) were not identified in all samples.

XRD Group 3. It corresponds to fabric 3 samples. This group is characterized by the presence of quartz (abundant), and calcite (abundant). Other minor mineralogical phases attributed to this group are illite-muscovite (scarce to traces), potassium feldspar (scarce to moderate), and plagioclase (scarce). Hematite (scarce to traces), anatase (scarce), and goethite (scarce) were not identified in all samples.

XRD Group 4. It corresponds to fabric 4 after OM observations. In this group, quartz is (very abundant) the dominant mineralogical phase, in

addition to illite-muscovite (moderate to abundant), potassium feldspar (scarce to moderate), and plagioclase (moderate to trace). Goethite (scare), hematite (scarce), and calcite (scare to trace) were not observed in all samples.

XRD results confirm OM observations, and clear differences in the semiquantitative amount of specific mineralogical phases suggest the exploitation of different raw materials to produce ceramics.

Regarding XRD group 1 and XRD group 3, they both show the presence of calcite and quartz. However, the dominance of calcite in XRD group 1 if compared to XRD group 3 clearly distinguishes them. Additionally, quartz is more abundant on samples categorized under XRD group 3 than in XRD group 1. Aside from these differences, other mineral phases, such as goethite and anatase, appear in the diffraction patterns of XRD group 3 samples. Still, they are never present in the XRD group 1 sample.

XRD results also clearly indicate disparities between XRD group 2 and XRD group 4. Although both groups are rich in quartz, the appearance of biotite, amphiboles, and talc in the diffraction patterns of XRD group 2, which are absent in XRD group 4, clearly differentiate these groups. Therefore, results indicate that the raw material employed to produce these ceramics was originally different. In the first case, the raw material probably developed from the weathering of "mafic" rock. Or, in the second case, the raw material perhaps developed from the alteration of a slightly different rock, containing few mafic minerals, and more felsic ones. This explains why, after OM observation, on fabric 4 ceramic samples biotite could be present, but it is not as abundant as muscovite.

The XRD result also corroborates some of the OM observation regarding the firing temperature employed for producing XRD group 1 and XRD group 3 ceramic samples. In XRD group 1 and 3 samples, the illite-muscovite peaks were identified. Considering that it begins to decompose at a temperature above 800° C (Humberto De Araújo *et al.* 2004) and it normally disappears above 950° C (Duminuco *et al.* 1998; Cultrone *et al.* 2014; el Ouahabi *et al.* 2015), it is possible to suggest that the maximum firing temperature was below the maximum limit (i.e., 950° C). Moreover, the presence of hematite in some of the ceramic samples of these two XRD groups suggests that ceramic samples could also be fired at a temperature of 750° C or more, considering that hematite generally start to nucleate at this temperature (Duminuco *et al.* 1998; Riccardi *et al.* 1999). In any case, the presence of very abundant to moderate amounts of calcite mineralogical phases in XRD patterns, and the identification of big calcite crystals (fabric 1) and limestone fragments (fabric 3) by optical microscopy, clearly indicate that a high firing temperature could be attained during ceramic firing, but it was not sufficient to destroy/digest calcite crystals and limestone fragments in the ceramic paste. This is because calcite crystals/limestone fragments are big in sizes, and this characteristic slows down the decarbonisation process in both cases, and thus, they can remain almost unaltered in the ceramic paste until 800°C (Rice 2005; Fabbri *et al.* 2014). In our case, some of the calcite crystals are fractured (i.e. fabric 1), but their original shapes are intact. Therefore, after these observations, it is suggested that XRD group 1 and 3 ceramics were probably fired in a temperature range comprised between 700 and below 950°C.

Regarding the firing temperature of XRD group 2 ceramic samples, kaolinite (moderate to scarce) mineral appears in two samples' diffraction patterns, meaning that the firing temperature could be lower than 550° C. Besides, kaolinite normally loses its crystalline structure at a temperature above 550° C (Velde & Druc 1999; Drebushchak *et al.* 2005). Also, in this group, hematite (scarce) appears in the diffraction patterns of some samples, suggesting that ceramics could be fired at, or above, 750° C (Duminuco *et al.* 1998; Riccardi *et al.* 1999). The presence of illite-muscovite (abundant to moderate) in XRD group 2 samples also indicate that the firing temperature was surely lower than 950° C, because illite-muscovite normally preserve its structure until 950° C (Duminuco *et al.* 1998; Cultrone *et al.* 2014; el Ouahabi *et al.* 2015). The presence of talc in some of the samples, corroborates this observation, because this mineralogical phase normally disappears at 895°C (Liu *et al.* 2014). So, one can infer that the firing temperatures of XRD group 2 ceramic samples range between 500° C and below 900° C.

As for the firing temperature of XRD group 4 ceramic samples, the detection of (abundant to moderate) illite-muscovite peaks indicate that ceramics were fired at a temperature below 950° C (Duminuco *et al.* 1998; Cultrone *et al.* 2014; el Ouahabi *et al.* 2015). The hematite peaks identified in some cases also suggest that the firing temperature could be above 750° C, because hematite starts to nucleate at 750° C (Duminuco *et al.* 1998; Riccardi *et al.* 1999). Therefore, with the presence of (abundant to moderate) illite-muscovite and (scarce) hematite in the XRD group 4 ceramic samples, one can suggest that potters fired XRD group 4 ceramic samples at a temperature between 700° C and below 950° C.

So, generally, ceramic samples firing temperature could range between 500° C and 950° C. The large firing range indicates the application of a rudimental firing technology, maybe using bonfires. By using this technology high temperature could be attained, but only for a short period. In terms of discontinuity or changes in the raw materials utilized for producing all the samples, XRD results suggest a discontinuity, thereby corroborating OM observations.

Table 3. Mineralogical species identified by XRD diffraction: Qtz, quartz; CAL, calcite, ILL-MUS, illite-muscovite; KAO-kaolinite; KF-potassium feldspar; PLA-plagioclase; DOLO, dolomite; AMP, amphibole; TAL, talc; GOE, goethite, HAL, halite; ANA, anatase; HEMA, hematite. ****-very abundant; ***-abundant; **- moderate; *-scarce; TR-traces.
Tabela 3. Espécies mineralógicas identificadas por DRX: QTZ, quartzo; CAL, calcita, ILL-MUS, llita-muscovita; KAO-Caulinite; KF-Feldspato de Potássio; PLA-Plagioclásio; DOLO, dolomita; AMP, anfíbola; TAL, talco; GOE, goethita, HAL, halita; ANA, anatase; HEMA, hematita. ****-muito abundante; ***-abundante; **- moderado; *-escasso; TR-vestígios.

S/N	Fabric	XRD group	QTZ	CAL	ILLI-MUS	KA0	KF	PlA	DOLO	BIO	AMP	TAL	GEO	HAL	ANA	HEMA
AVE S1	1	1	*	****	*											
AVE S2	2	2	****		**		**	**		*						*
AVE S3	2	2	****	*	**		*	*		*	*					
AVE S4	3	3	****	**	**		**						*		*	*
AVE S5	4	4	****		**		*	*								*
AVE S6	3	3	****	*	*		TR	**							*	
AVE S7	2	2	****		***		**	*		**						
AVE S8	1	1	**	****	TR		TR	TR							*	
AVE S9	2	2	****		**	**	*	**		*	**	**				
AVE S10	1	1	**	****	**		*			*						*
AVE S11	2	2	****		**		*	**		*	*					*
AVE S12	2	2	****		**		*	**		*	*		*			*
AVE S13	3	3	****	**	TR		*								*	*
AVE S14	2	2	****	TR	**	*	*	**		*	**	**				
AVE S15	1	1	**	****	*				*							*
AVE S16	2	2	****		**		*	**			**					*
AVE S17	3	3	****	**	*		*	*								TR
AVE S18	1	1	*	****	*											
AVE S19	4	4	****		**		*	TR								
AVE S20	1	1	**	****	*											
AVE S21	4	4	****		**		**	TR								TR
AVE S22	2	2	****		**		***	*			*	*				
AVE S23	2	2	****		**		*	***		*	*	*				

Table 3. Mineralogical species identified by XRD diffraction: Qtz, quartz; CAL, calcite, ILL-MUS, illite-muscovite; KAO-kaolinite; KF-potassium feldspar; PLA-plagioclase; DOLO, dolomite; AMP, amphibole; TAL, talc; GOE, goethite, HAL, halite; ANA, anatase; HEMA, hematite. ****-very abundant; ***-abundant; **- moderate; *-scarce; TR-traces (cont).
Tabela 3. Espécies mineralógicas identificadas por DRX: QTZ, quartzo; CAL, calcita, ILL-MUS, llita-muscovita; KAO-Caulinite; KF-Feldspato de Potássio; PLA-Plagioclásio; DOLO, dolomita; AMP, anfíbola; TAL, talco; GOE, goethita, HAL, halita; ANA, anatase; HEMA, hematita. ****-muito abundante; ***-abundante; **- moderado; *-escasso; TR-vestígios (cont).

AVE S24	**1**	**1**	**	** **	**TR**									*	TR	
AVE S25	**1**	**1**	**	** **	*											
AVE S26	**4**	**4**	** **	*	**		* *	**T R**					*			*
AVE S27	**4**	**4**	** **		** *		*	* *								
AVE S28	**1**	**1**	** **	**	*											
AVE S29	**1**	**1**	**	** **												
AVE S30	**1**	**1**	**	** **	**		*	*								
AVE S31	**1**	**1**	*	** **	*		*									
AVE S32	**1**	**1**	*	** **	*											
AVE S33	**1**	**1**	**	** **	*		*	*								*
AVE S34	**1**	**1**	**	** **	*											*
AVE S35	**3**	**3**	** **	** **	*			*								*
AVE S36	**1**	**1**	** *	** **	*		*									*
AVE S37	**1**	**1**	**	** **	*											
AVE S38	**3**	**3**	** **	**	**		*	*								*
AVE S39	**4**	**4**	** **	**T R**	**		*	* *								*
AVE S40	**4**	**4**	** **		**		*	* *								*
AVE S41	**4**	**4**	** **		**		*	*								*
AVE S42	**3**	**3**	** **	**	*		*	*								

5.3. X-Ray Fluorescence (XRF)

XRF results (see annexes) corroborate optical microscopy and X-ray diffraction (XRD) results, indicating different ceramic samples provenance. Calcium and strontium are extremely important in our case. Besides, strontium may/ generally substitutes calcium in calcium rich mineralogical phases, so the ratio between these two different chemical elements can give useful information about ceramic samples origin. As it can be clearly seen in figure 8A, Ca/Sr ratio and Fe are inversely correlated. This indicates that, as soon as Fe content decreases, Ca/Sr ratio increases accordingly.

Samples included in fabric 1 (i.e., XRD group 1) are enriched in calcite crystals; fabric 3 samples (i.e., XRD group 3) are enriched in limestone fragments; fabric 2 and 4 samples (i.e., XRD groups 2 and 4) are poor in calcium-rich minerals if compared to fabric 1 and 3 samples. The only mineralogical phases incorporating Ca and Sr in fabric 2 and 4 are plagioclase feldspars, calcite (i.e., scarce to trace), only identified in 5 out of 18 samples by XRD, amphiboles (just in fabric 2), and possibly, clay minerals.

As for the Ca/Sr ratio in fabric 1 and 3, the ratio shows that Sr content does not increase as Ca content increases within fabrics. In the case of fab-

ric 1 samples, calcite is the main mineralogical phase that can incorporate Sr within its crystalline structure. The ratio is very high (ratio= 4224 to 1386), indicating that calcite crystals in fabric 1 samples are Sr poor. The same reasoning is valid for fabric 3 samples, which are enriched in limestone fragments. Of course, calcite is the main component of limestone, but in this case big calcite crystals are not present, and as a result, the Ca/Sr ratio difference decreases (i.e., not as high as that of fabric 1) (ratio = 1739 to 387). This show that Sr content is higher in these samples (i.e., fabric 3) compared to fabric 1 ceramics. So, even if "calcite" is always present in both cases, the ratio is extremely different suggesting that calcite crystals diagenesis was also different in the two cases, influencing Sr concentration in fabric 1 ceramic samples (Veizer 1978; Perrin *et al.* 2014).

For fabric 2 and 4, Ca/Sr ratio is much lower (ratio = 197 to 25), and calcite mineral was rarely identified in XRD patterns in both fabrics, as already stated. This suggest that Ca is mostly hosted by a plagioclase feldspar (i.e. considering XRD results). They were clearly identified by XRD in both cases and, remarkably, Sr content is higher if compared to calcite crystals observed in fabric 1, and calcite in limestone from fabric 3. So, in these cases the Ca/Sr ratio is diagnostic, and indicates

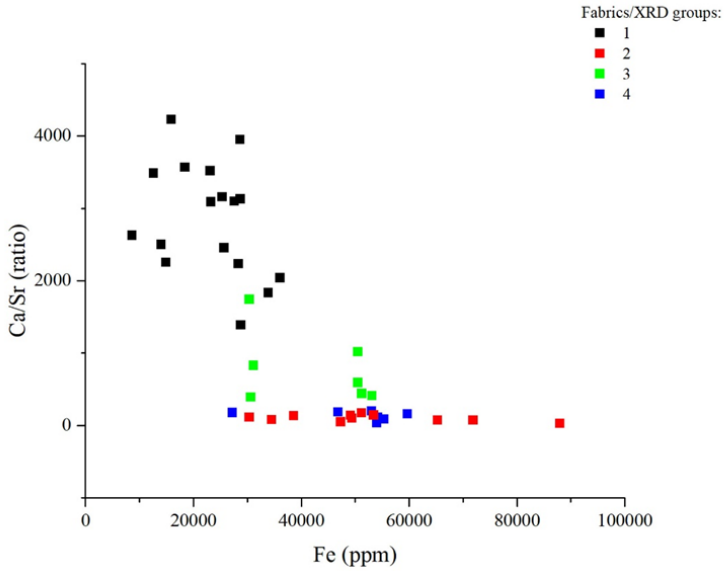

A

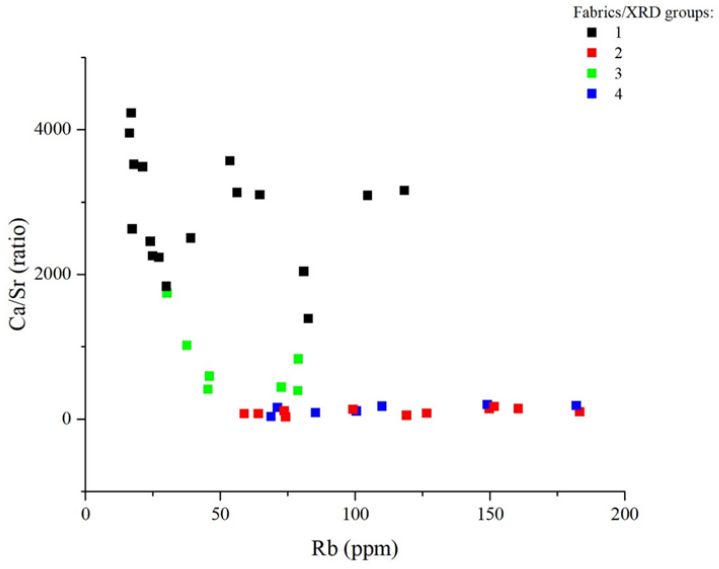

B

Fig. 8A/B. Ca/Sr ratio vs Fe and Ca/Sr ratio vs Rb binary plots of ceramic samples included in this study.
Fig. 8A/B. Gráficos binários razão Ca/Sr vs Fe, e razão Ca/Sr vs Rb das amostras de cerâmicas incluídas neste estudo.

different raw material sources, supporting OM and XRD results.

The same subdivision is proven by the binary plot presented in figure 8B. In this case Fe has been substituted by Rb in the binary plot. This chemical element generally substitutes K phases such as potassium feldspars, and micas (HEINRICHS *et al.* 1980). This indicates that fabric 2 and 4 are also tendentially enriched in Rb hosting minerals if compared to fabric 1 and 3 samples.

Difference in raw materials is also evident in the binary plots presented in figures 9A and 9B. As showed by OM and XRD results for fabrics 1, 2, 3 and 4 evidenced that calcite (CaO) and quartz (SiO_2) are important mineralogical phases. SiO_2 *vs* CaO binary plot clearly show (9B) that fabric 2 and 4 are silica rich. The situation is different for fabric 1, that is silica poor. Fabric 3 is enriched in SiO_2 if compared to fabric 1. Similar observations were developed in the OM and XRD sections.

The binary plot of figure 9A also evidenced differences in Al_2O_3 and SiO_2 content between fabrics. Al and Si are mostly hosted by phyllosilicates (i.e., clay minerals and micas), feldspars and quartz. So, this plot clearly indicates a difference in Al and Si rich mineralogical phases within fabrics. Fabric 1 is poor in both oxides if compared to fabric 3, and this is because fabric 3 possesses more k-feldspars and quartz as confirmed by OM and XRD observations. In the case of fabric 2 and 4, the

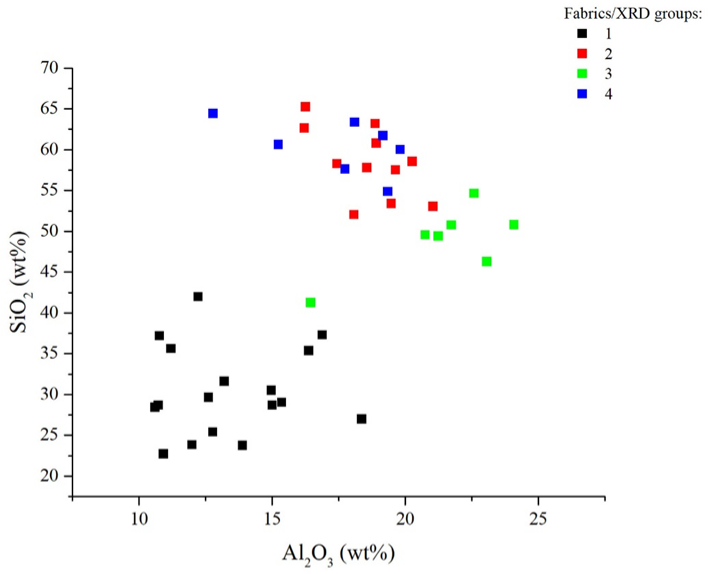

A

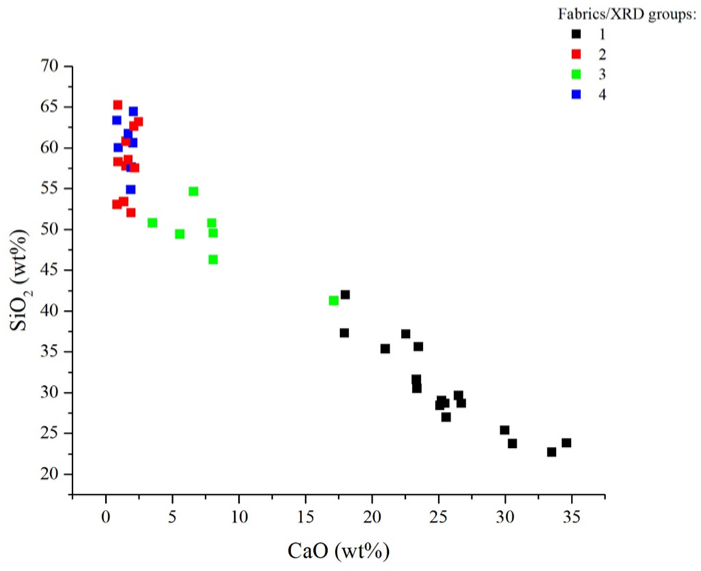

B

Fig. 9A/B. SiO_2 vs Al_2O_3 and SiO_2 vs CaO binary plots of ceramic samples included in this study.
Fig. 9A/B. Gráficos binários SiO_2 vs Al_2O_3, e SiO_2 vs CaO das amostras de cerâmicas incluídas neste estudo.

identification of Al and Si rich mineralogical phases by OM and XRD confirms their enrichment in both oxides.

Nevertheless, observations do not clearly distinguish fabric 2 and 4 ceramic samples. In this case the ternary plot (Fig. 10) subdivides samples basing on CaO, MgO and Fe_2O_3 normalized content. The main difference between fabric 2 and 4 resides in MgO concentration. In this case, fabric 2 is enriched in biotite, and to some extent by amphiboles and talc, which host Mg in their crystalline structure (KLEIN 2002). Conversely, fabric 4 is enriched in muscovite after OM and XRD analyses. So, fabric 2 is enriched in MgO hosting mineralogical phases if compared to fabric 4.

Just in one fabric 4 sample (i.e., sample R28-528) MgO concentration is high, if compared to the rest of the group. Petrography and XRD results showed that no Mg rich mineralogical phases were present in the ceramic body. So, in this case MgO was probably concentrated in the ceramic paste. SEM-EDS will be the best option to evaluate this characteristic.

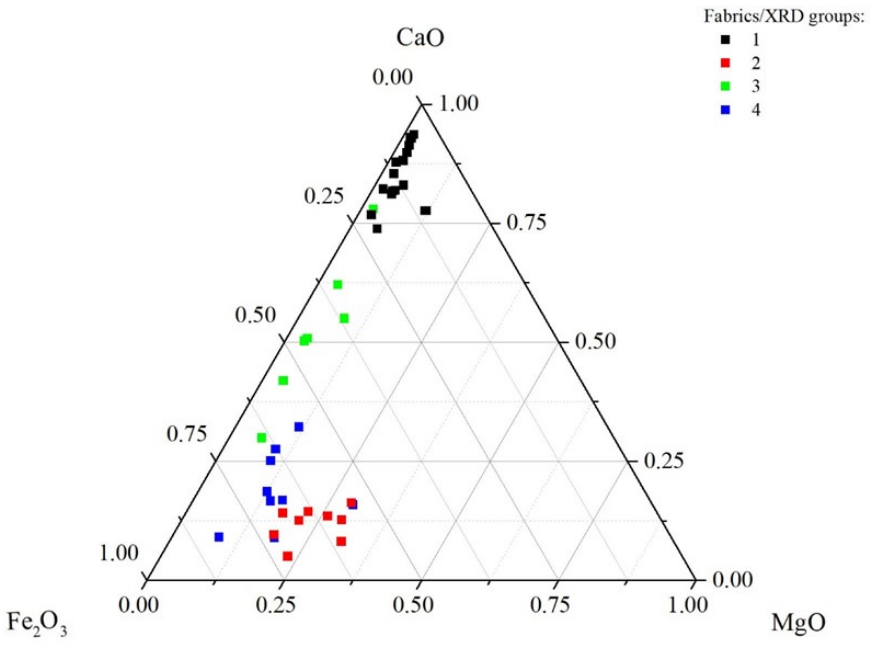

Fig. 10. CaO – MgO – Fe_2O_3 ternary plot of ceramic samples included in this study.
Fig. 10. Gráfico ternário CaO – MgO – Fe_2O_3 das amostras de cerâmicas incluídas neste estudo.

5.4 SEM-EDS

SEM-EDS results confirmed XRD, OM, and XRF observations. Backscattered electron (BSE) images, Secondary Electron (SE) images, elemental distribution maps, and punctual chemical analysis were collected, and new information were added for the characterization of the ceramic samples.

As for fabric 1 (i.e., XRD group1), 4 samples (i.e., samples: P28-211, Q28-578, Q28-713, Q28-727, R27-478) out of 17 were analysed to evaluate the elemental distribution within ceramic paste and temper. The SEM-EDS analysis (Fig. 11) results indicate that the fabric's tempers are mainly composed of calcium-rich crystals (i.e., calcite identified in the OM and XRD). Conversely, the samples' matrices are rich in silicon, aluminum, and potassium. So, calcite crystals are the main mineralogical phases that contribute to the CaO concentration of the samples' chemical compositions (i.e., obtained by XRF).

However, in one case (i.e., in sample Q28-579), dolomite was clearly detected by XRD but not identified by OM. Microanalysis (Fig. 12, 13) reveals that magnesium is an essential chemical element in this case. Besides, the ceramic body chemical mapping of sample Q-28-579 proves that calcite grains could include Mg-rich domains.

The microanalysis (i.e. punctual analysis) evidenced that Mg rich domains inside calcite crystals (Fig. 13) contain 20.86 wt% of MgO, and 49.78 wt% of CaO. Conversely, Ca-rich area in the same crystal contain 0.83 wt% of MgO, and 79.47 wt% of CaO. So, in this case, it is possible to state that dolomite (i.e. also identified by XRD) is included in some calcite crystals. This observation slightly differentiates this sample within fabric 1. It is also important to emphasize that dolomite inclusion inside calcite crystals was not observed during OM observations. So, combining optical microscopy and different analytical (i.e., XRD and SEM-EDS) techniques was fundamental to characterize this sample. Regarding the sample's paste (i.e., matrix), it is also enriched in aluminium, silicon, and potassium (Fig. 12), indicating that calcium and magnesium contribution to the chemical composition of the ceramic paste is low.

In the case of fabric 2, 4 out of 10 samples were analysed by SEM-EDS. The analysed samples (i.e., samples P27-604, R27-465, R28-609,

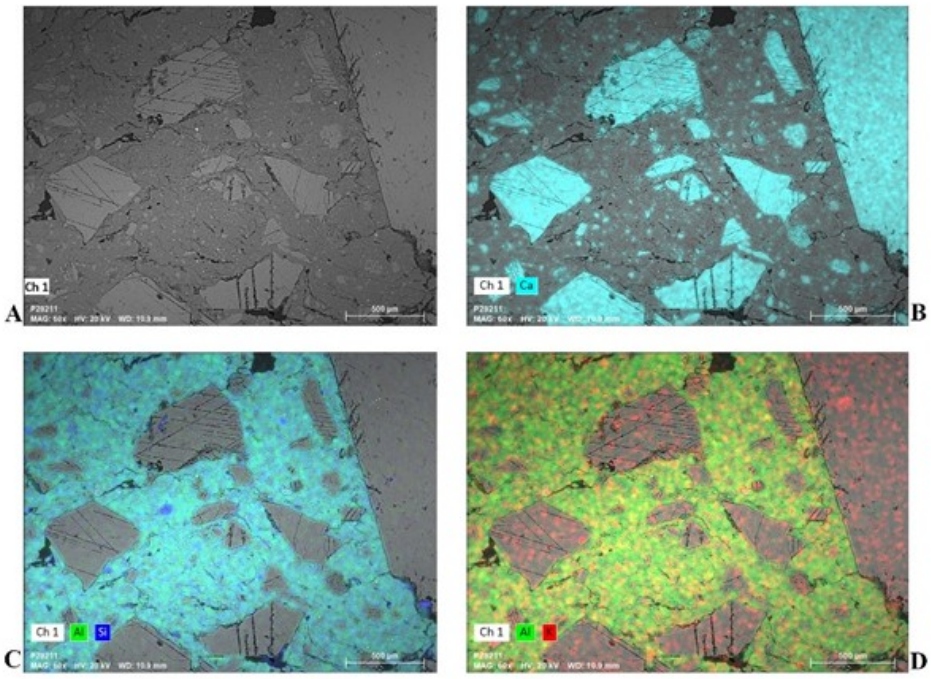

Fig. 11. A) Representative BSE image of fabric 1 (Sample P28-211). B) Elemental distribution map of calcium (Ca). C) Elemental distribution map of aluminium (Al) and silicon (Si). D) Elemental distribution map of aluminium (Al) and potassium (K).
Fig. 11. A) Imagem BSE do fabrico 1 (Sample P28-211). B) Mapa de distribuição elementar do cálcio (Ca). C) Mapa de distribuição elementar do alumínio (Al) e do silício (Si). D) Mapa de distribuição elementar do alumínio (Al) e do potássio (K).

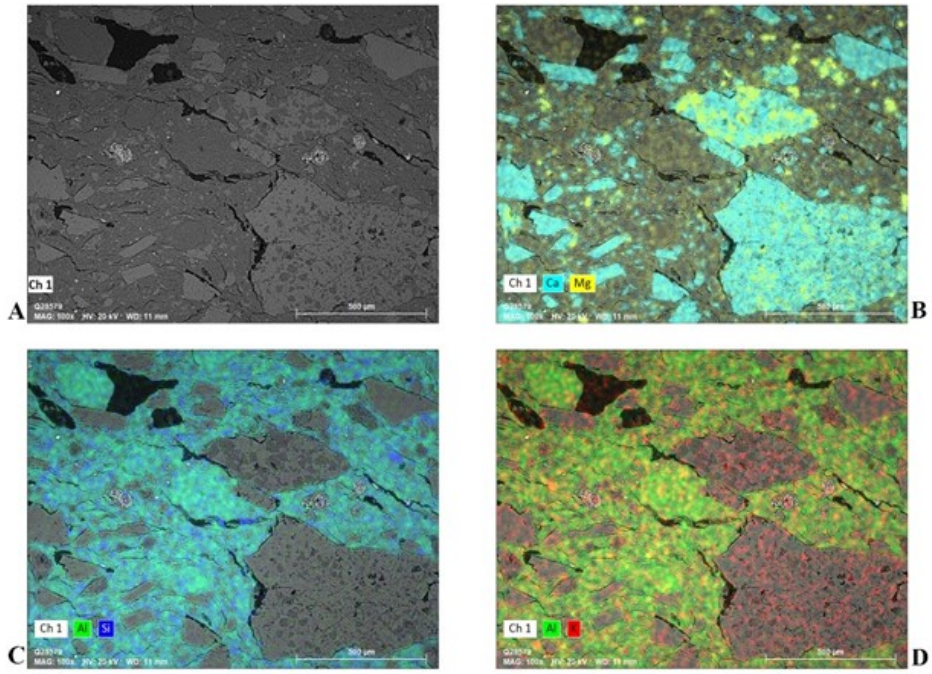

Fig. 12. A) BSE image of sample Q28-579. B) Elemental distribution map of calcium (Ca) and magnesium (Mg). C) Elemental distribution map of aluminium (Al) and silicon (Si). D) Elemental distribution map of aluminium (Al) and potassium (K).
Fig. 12. A) Imagem BSE da amostra Q28-579. B) Mapa de distribuição elementar do cálcio (Ca) e do magnésio (Mg). C) Mapa de distribuição elementar do alumínio (Al) e do silício (Si). D) Mapa de distribuição elementar do alumínio (Al) e do potássio (K).

and R27-510) of the fabric show a different elemental distribution in the ceramic paste and temper if compared to fabric 1. Silicon is mostly hosted by big temper grains of quartz, as seen in the picture in figure 14. This is not surprising because OM and XRD analysis also identified quartz as the dominant mineralogical phase of this fabric. Potassium, iron, and magnesium are mainly hosted by fibrous and elongated minerals. Besides, biotite was identified during OM observations and XRD analyses. Muscovite can also be identified in the picture. The habit of muscovite is very similar to that of biotite crystals, but they are enriched in potassium as depicted in the collected elemental distribution map (Fig. 14C). In the case of feldspars crystals of fabric 2 samples, they are tendentially enriched in sodium and calcium, indicating that they are generally plagioclase feldspars. Distribution elemental mapping and punctual analysis showed that alkali feldspars are less represented if compared to plagioclase feldspars (Fig. 15).

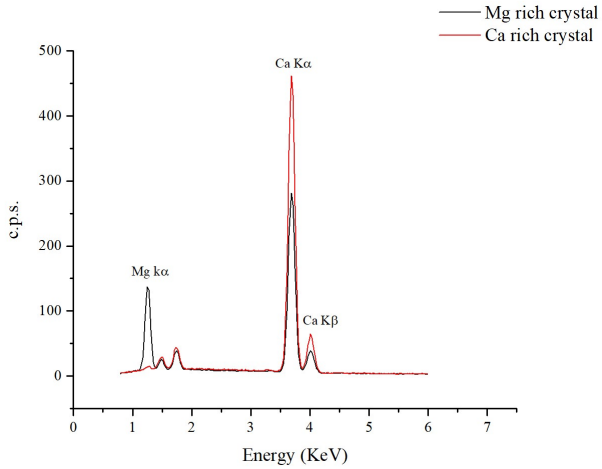

Point (chemical composition) Analysis			
Ca-rich crystal		**Mg-rich crystal**	
Oxide	**wt. %**	**Oxide**	**wt. %**
CaO	20.86	CaO	0.83
MgO	49.78	MgO	79.47

Fig. 13. Spectrum obtained using SEM-EDS of Ca and Mg rich domains in sample Q28-579, and quantitative data for CaO and MgO.
Fig. 13. Espetro obtido por SEM-EDS de domínios enriquecidos em Ca e Mg na amostra Q28-579, e dados quantitativos por CaO e MgO.

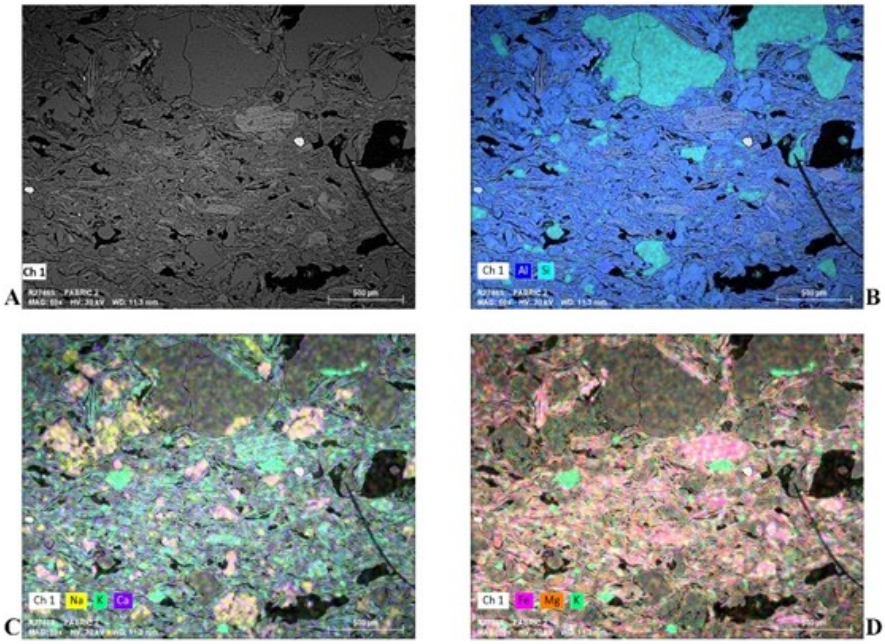

Fig. 14. A) BSE image of Sample R27-465. B) Elemental distribution map of aluminium (Al) and silicon (Si). C) Elemental distribution map of sodium (Na), potassium (K), and calcium (Ca). D) Elemental distribution map of iron (Fe), magnesium (Mg), and potassium (K).
Fig. 14. A) Imagem BSE da amostra R27-465. B) Mapa de distribuição elementar do alumínio (Al) e do silício (Si). C) Mapa de distribuição elementar do sódio (Na), potássio (K) e do cálcio (Ca). D) Mapa de distribuição elementar do ferro (Fe), magnésio (Mg), e do potássio (K).

Regarding fabric 3, SEM-EDS analyses were performed on 2 (i.e., samples: Q28-877 and R28-540) out of 6 samples. Results show that samples ceramic pastes are enriched in aluminium, silicon, and lessly by potassium (Fig. 16). The elemental distribution maps of the fabric also reveal that silicon and calcium are the major chemical elements distributed and concentrated in the inclusions of fabric 3, thereby confirming OM observations. Potassium-rich feldspars could also be rarelly observed.

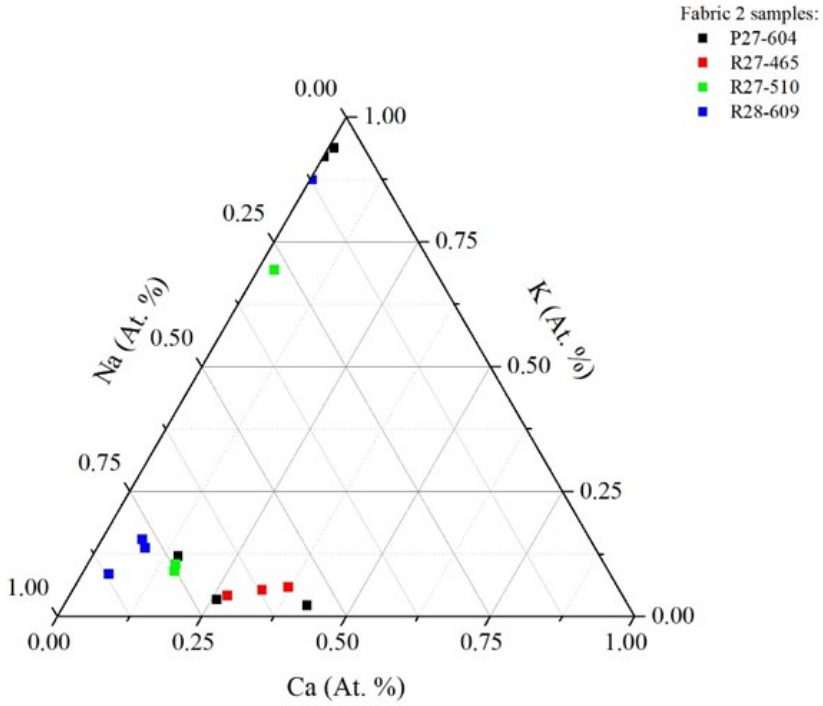

Fig. 15. Feldspars ternary diagram of fabric 2 samples (data obtained after punctual chemical analysis).
Fig. 15. Gráfico ternário dos feldspatos das amostras do fabrico 2 (dados obtidos por analise química pontual).

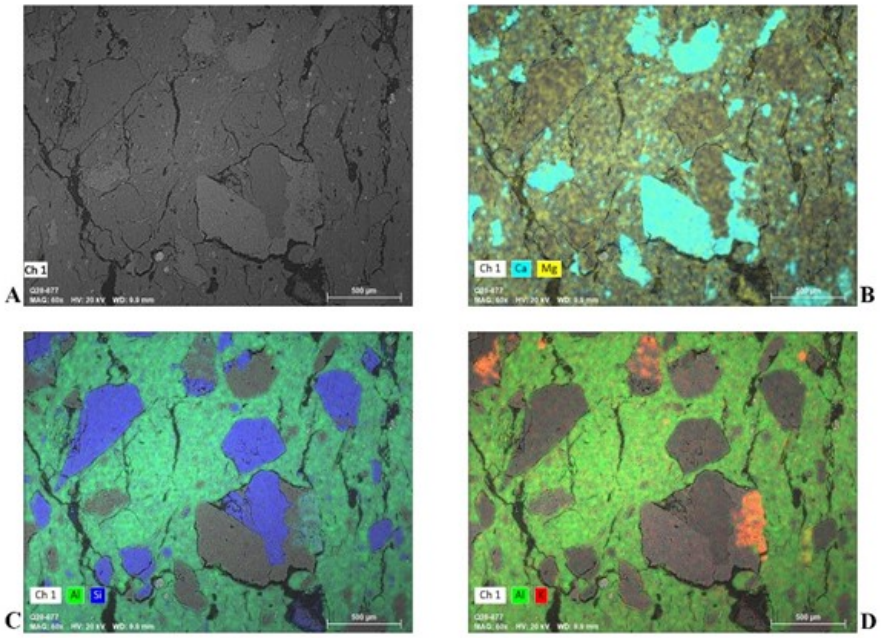

Fig. 16. A) BSE image of Sample Q28-877 B) Elemental distribution map of calcium (Ca) and magnesium (Mg). C) Elemental distribution map of aluminium (Al) and silicon (Si). D) Elemental distribution map of aluminium (Al) and potassium (K).
Fig. 16. A) Imagem BSE da amostra Q28-877. B) Mapa de distribuição elementar do cálcio (Ca) e do magnésio (Mg). C) Mapa de distribuição elementar do alumínio (Al) e do silício (Si). D) Mapa de distribuição elementar do alumino (Al) e do potássio (K).

Regarding fabric 4, 4 samples (P27-201, P28 -620, Q27-161, and R28-528) out of 8 were analysed by SEM-EDS. The elemental mappings of the analysed samples also indicate that silicon is mostly hosted by big temper grains of quartz (Fig. 17). Besides, quartz was always identified by OM and XRD, and it represents the dominant mineralogical phase of this fabric. Iron, magnesium, calcium, and aluminium are the main chemical elements included in the ceramic paste of the fabric. Iron, magnesium, calcium, and aluminium are the main chemical elements included in the ceram-

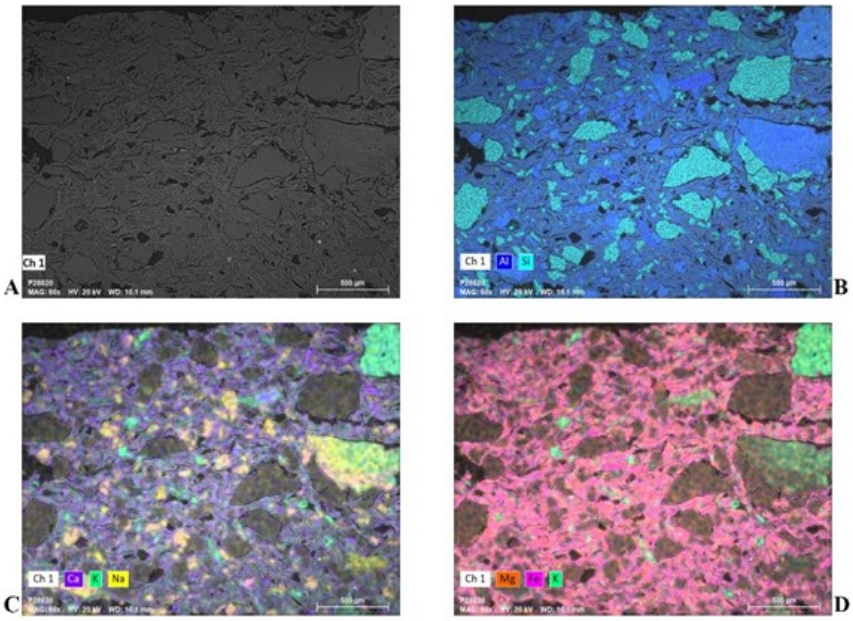

Fig. 17. A) BSE image of Sample P28-620 B) Elemental distribution map of aluminium (Al) and silicon (Si). C) Elemental distribution map of sodium (Na), potassium (K), and calcium (Ca). D) Elemental distribution map of iron (Fe), magnesium (Mg), and potassium (K).
Fig. 17. A) Imagem BSE da amostra P28-620. B) Mapa de distribuição elementar do alumínio (Al) e do silício (Si). C) Mapa de distribuição elementar do sódio (Na), potássio (K) e do cálcio (Ca). D) Mapa de distribuição elementar do ferro (Fe), magnésio (Mg), e do potássio (K).

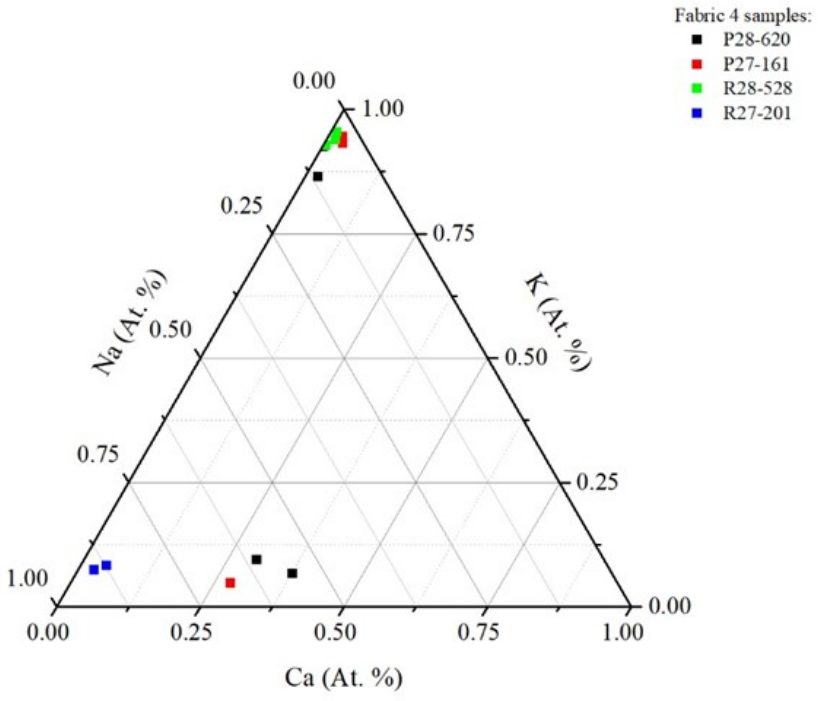

Fig. 18. Feldspars Ternary diagram of fabric 4 samples (data obtained after punctual chemical analysis).
Fig. 18. Gráfico ternário dos feldspatos das amostras do fabrico 4 (dados obtidos por analise química pontual).

ic paste of the fabric. Conversely, potassium is embedded in fibrous and elongated minerals which can be classified as muscovite. On rare occasions, in this fabric, crystals of biotite enriched in potassium, iron, and magnesium could also be observed. Moreover, XRF revealed high MgO concentration on samples R28-528 if compared to the rest of fabric 4 specimens. The elemental mapping distribution of the ceramic body evidenced that MgO is mainly concentrated in the ceramic paste and not in the temper. This indicates that the raw material employed to produce ceramic included in fabric 4 could be heterogeneous. In the case of feldspars crystals of fabric 4 samples, they are primarily enriched in sodium and potassium if compared to fabric 2 samples, indicating that both potassium feldspars and plagioclase feldspars are present (Fig. 18).

5.5. Helium Pycnometry

The physical properties of the ceramic fragments show heterogeneous results. Mean values are presented in table 4, while singular values for each sample are presented in the annexed file. Considering ceramic fabrics, the mean values for total porosity (Φ_T) make the first difference. As it can be clearly seen in (Fig. 19), fabric 1 show the lowest values of total porosity. On the contrary, fabric 2 samples show the highest values of total porosity, while fabric 3 and 4 show intermediate/similar values (i.e., fabric 4 show slightly higher values if compared to fabric 3). Normally ceramic total porosity can be influenced by temper amount and size. In this case porosity is higher when the piece has big inclusions and temper amount is considerable. This favours the formation of structural discontinuities between temper grains and the ceramic paste (Allegretta *et al.* 2014). The firing temperature also influence this physical property, and porosity normally decreases when the firing temperature increases as a consequence of the vitrification of the ceramic paste. Moreover, it can also be influenced by the pressure made by the potter when modelling the pot and kneading the paste, or by surface treatment/slip application.

Considering temper size and amount, fabric 1 show the highest average values of temper concentration (Table 4), if compared to fabrics 2, 3 and 4. Fabrics 2, 3, and 4 also show higher standard deviation. Fabric 1, 3 and 4 showed lower values of maximum temper grain size if compared to fabric 2. So, temper concentration and maximum temper grain size, in our case, do not fully explain samples total porosity amount.

To further discuss this property, the effect of the firing temperature on the characteristic of the clay matrix is widely discussed in the bibliography (Kam *et al.* 2009; de Bonis *et al.* 2014; Beltrame *et al.* 2020a), and when the firing temperature increases, the open porosity generally decreases. The plot presented in figure 20, suggests that ceramics were probably fired at different temperature, because they show different values of open porosity to helium and water. The proposed temperature range for fabric 1, 2, 3, and 4 are included in table 4 (i.e., evaluated after XRD interpretation).

Fabric 2 presents the biggest interval of firing temperature, indicating they could have been

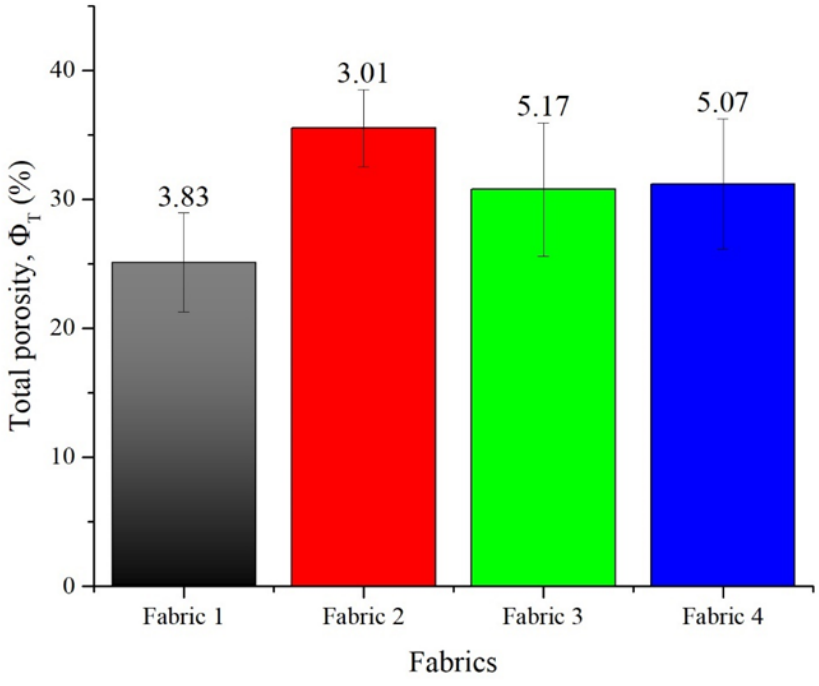

Fig. 19. Graphical representation of total porosity medium values with standard deviation of each fabric.
Fig. 19. Representação gráfica dos valores médios da porosidade total com desvio padrão de cada fabrico.

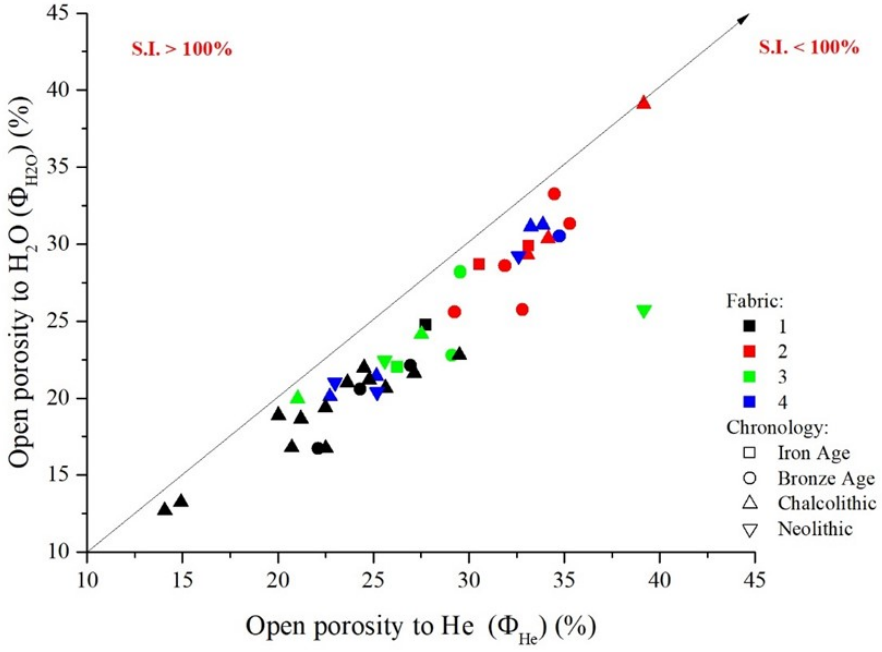

Fig. 20. Binary plot of open porosity to water vs. open porosity to helium.
Fig. 20. Gráfico binário da porosidade aberta a água vs a porosidade aberta ao hélio.

Table 4. Mean values of the physical properties for each fabric.
Tabela 4. Valores médios das propriedades físicas de cada fabrico.

Samples		Temper		Apparent density	Real density	Solid density	Total porosity	Open porosity to water	Open porosity to helium	Closed porosity to helium	Weight imbibition coefficient	Saturation index	Estimated firing temperature (XRD)
				ρ_B	ρ_R	ρ_S	ΦT	ΦH_2O	ΦHe	ΦcHe	IC_w	IS	
		2D %	Max grain size (mm)	(g/cm^3)	(g/cm3)	(g/cm^3)	(%)	(%)	(%)	(%)	(%)	(%)	°C
Fabric 1	Mean	23.88	3.4	2.06	2.68	2.74	25.13	19.40	23.07	2.06	9.44	84.26	700-950
	St.Dev.	3.29		0.07	0.07	0.06	3.83	3.19	4.03	1.74	1.83	5.54	
Fabric 2	Mean	19.74	5.5	1.79	2.68	2.74	35.53	30.18	33.39	2.14	17.13	89.96	500-900
	St.Dev.	12.25		0.14	0.14	0.14	3.01	3.70	2.58	1.55	3.90	5.44	
Fabric 3	Mean	21.79	3.6	1.89	2.63	2.70	30.80	23.61	28.32	2.48	12.62	84.54	700-950
	St.Dev.	9.44		0.13	0.05	0.06	5.17	2.50	5.14	1.26	2.09	9.54	
Fabric 4	Mean	20.08	2.2	1.88	2.64	2.70	31.20	25.63	28.81	2.38	13.74	88.45	700-950
	St.Dev.	12.42		0.07	0.09	0.10	5.07	4.95	4.91	1.85	3.13	3.82	

fired at a lower temperature if compared to fabric 1,3, and 4. Besides, kaolinite was identified on some samples included in this fabric.

In the case of fabric 1 and 3, ceramics were probably fired at higher temperature, and the estimated firing temperature range is also smaller if compared to fabric 2. Besides, the identification of big calcite crystals and limestone fragments inside the ceramic paste might suggest that the firing temperature could be as high as 800 °C (Rice 2005; Fabbri *et al.* 2014). Nevertheless, hematite (which crystalizes from 750 °C) was not systematically identified by XRD both in fabric 1 and 3 (see in XRD part). In the case of fabric 4, results are heterogeneous, and the established firing temperature range is between 700 and 950 °C (i.e. similarly to fabric 1 and 3). Besides, a group of specimens show similar characteristic to fabric 1 and 3 samples. For example, samples R28-528, R28-604, P27-201 and P27-106 have hematite (based on XRD observation), which also appear in some of the fabric 1 and 3, suggesting higher firing temperature and consequently a lower amount of open porosity to water and helium. In other cases, they show similar characteristic to fabric 2. So, it is only possible to suggest that the firing temperature of fabric 4 is probably more heterogeneous.

6. CONCLUSION AND REMARKS

This study determined the characteristics of the raw materials employed by ancient potters to produce ceramic samples, the possible raw material sources, the ceramic firing temperature, possible change in the raw materials exploitation between the Neolithic and the Iron Age and, lastly, the physical properties of each sample/fabric.

As for ceramic technology (i.e., the raw materials) of each fabric, results revealed that potters employed different raw materials to produce fabrics. Fabric 1 was manufactured using calcite as main tempering material. Fabric 2 samples were produced with silica-mica-rich raw material, being enriched in quartz, biotite, and to some extent in amphiboles and talc. Fabric 3 samples were mainly manufactured using limestone fragments and quartz as tempering materials. Fabric 4 was produced with silica-mica-rich raw materials, being enriched in quartz and muscovite if compared to fabric 2.

Therefore, based on the above highlighted mineralogical components, and the information obtained on the geology of Avecasta area, it was observed that fabric 1 and 3 raw materials were obtained within Lusitanian Meso-Cenozoic Basin. Moreover, it is suggested that fabrics 1 ceramic samples were produced by the people who lived inside the cave, using calcite as main tempering material. Fabric 3 raw materials were obtained within the geological zone of Lusitania Basin, but we could not identify from which part of the Lusitanian Basin the raw material was collected. On the contrary, fabric 2 and 4 ceramic samples exhibit mineralogical characteristics compatible with the geological outcrops of the PTSZ/CIZ zones. So, it is suggested that the raw materials employed by potters to produce the ceramic samples of fabric 2 and 4 were collected within this area at maximum 10-15 km from the cave. Based on the submission of Rice that potters could travel as far as 24km to obtain clay and additives for producing ceramic (Rice 2005), it could thus be possible that people from the cave embarked on a journey to obtain tempering materials to produce fabric 2 and 4 ceramic samples. Conversely, it could also be that the ceramic sherds arrived at the Avecasta cave as a result of trade relations between the people who lived in the cave and their neighbours. Perhaps future archaeological/archaeometric studies on prehistory/protohistoric ceramics from the neighbouring proto-historic villages close to Avecasta can further shed light on these hypotheses.

Regarding ceramics firing temperature, our results indicate that ceramic samples were most probably fired at different temperatures. This observation also was suggested/indicated by physical properties evaluation. The porosity results of the forty-two ceramic samples show that fabric 2 and 4 ceramic samples tendentially exhibit high porosity amount if compared to fabric 1 and 3 samples.

Considering the production continuity/ discontinuity of each fabric between the Neolithic and the Iron Age, a discontinuity was observed in the raw materials utilized for ceramic production. Potters did not use fabric 1 and 2 raw materials during the Neolithic period, and never employed fabric 4 raw material for ceramic production in the Iron Age.

Finally, this research strength was limited by the unavailability of information on the typologies of ceramic samples from Avecasta and thus it was not possible to link our archaeometric results to any type of ceramics from Avecasta region. Nevertheless, this research has filled the gap of the absence of archaeometric studies of ceramics from cave settlements in the centre of Portugal. It also contributed to the ongoing Avecasta archaeological project by revealing the raw materials used in ceramic production recovered inside the cave and their sources.

7. BIBLIOGRAPHY

Allegretta, I., Eramo, G., Pinto, D. & Hein, A. 2014. The effect of temper on the thermal conductivity of traditional ceramics: Nature, percentage and granulometry. *Thermochimica Acta*, 581: 100–109.

Azerêdo, A. C. 2007. Formalização da litostratigrafia do Jurássico Inferior e Médio do Maciço Calcário Estremenho (Bacia Lusitânica). *Comunicações Geológicas*, 94:29-51.

Barnett, W. K. 1987. The physical analysis of Early Neolithic impressed pottery from Gruta do Caldeirão (Tomar, Portugal). *O Arqueólogo Português* 5: 67-87.

Beltrame, M., Sitzia, F., Liberato, M., Santos, H., Barata, F. T., Columbu, S. & Mirão, J. 2020. Comparative pottery technology between the Middle Ages and Modern times (Santarém, Portugal). *Archaeological and Anthropological Sciences* 12: 1-31.

Beltrame, M., Bottaini, C., Cruz, A., Vilaça, R. & Mirão, J., 2019. O Tumulus 1 do Souto (Abrantes,

Médio Tejo): Novos contributos para o conhecimento das materialidades do mundo funerário do Bronze Final no Centro de Portugal. *Estudos Do Quaternário/Quaternary Studies*, 19), 33–48. https://doi.org/10.30893/eq.v0i19.177.

Beltrame, M., Liberato, M., Mirão, J., Santos, H., Barrulas, P., Branco, F., Gonçalves, L., Candeias, A. & Schiavon, N., 2019. Islamic and post Islamic ceramics from the town of Santarém (Portugal): The continuity of ceramic technology in a transforming society. *Journal of Archaeological Science: Reports*, 23, 910–928. https://doi.org/10.1016/j.jasrep.2018.11.029.

Beltrame, M., Sitzia, F., Arruda, A. M., Barrulas, P., Barata, F. T. & Mirão, J., 2021. The Islamic Ceramic of the Santarém Alcaçova : Raw Materials, Technology, and Trade. *Archaeometry*, 63(6), 1157–1177. https://doi.org/10.1111/arcm.12671.

Cultrone, G., Molina, E. & Arizzi, A. 2014. The combined use of petrographic, chemical, and physical techniques to define the technological features of Iberian ceramics from the Canto Tortoso area (Granada, Spain). *Ceramics International*, *40*:10803–10816.

de Bonis, A., Cultrone, G., Grifa, C., Langella, A. & Morra, V. 2014. Clays from the Bay of Naples (Italy): New insight on ancient and traditional ceramics. *Journal of the European Ceramic Society*, 34: 3229–3244.

Delgado J. F. N. 1884. *La grotte de Furninha a peniche In congres International d'Anthropologie et d'Archeologie prehistorique a Lisbonne*, Lisboa. Typographie de l'Académie royale des sciences 1-35.

Drebushchak, V. A., Mylnikova L. N., Drebushchak T. N. & Boldyrev V. V. 2005. The investigation of ancient pottery. *Journal of Thermal Analysis and Calorimetry,* 82: 617–626.

Duminuco, P., Messiga, B. & Riccardi, M. P. 1998. Firing process of natural clays. Some microtextures and related phase compositions. *Therochimica Acta*, 321:185-190.

el Ouahabi, M., Daoudi, L., Hatert, F. & Fagel, N. 2015. Modified mineral phases during clay ceramic firing. *Clays and Clay Minerals*, 63: 404–413.

Fabbri, B., Gualtieri, S. & Shoval, S. 2014. The presence of calcite in archaeological ceramics. *Journal of the European Ceramic Society* 34: 1899–1911.

Heinrichs, H., Schulz-Dobrick, B. & Wedepohl, K. H. 1980. Terrestrial geochemistry of Cd, Bi, Tl, Pb, Zn and Rb. *Geochimica et Cosmochimica Acta*, 44: 1519–1533.

Humberto De Araújo, J., Francisco Da Silva, N., Acchar, W. & Gomes, U. 2004. Thermal Decomposition of Illite 359. *Materials Research* 7:359-361.

Kam, S., Zerbo, L., Bathiebo, J., Soro, J., Naba, S., Wenmenga, U., Traoré, K., Gomina, M. & Blanchart, P. 2009. Permeability to water of sintered clay ceramics. *Applied Clay Science*, 46:351–357.

Klein, C. 2002. *Mineral Sciences*. New York/Chichester/Weinheim/Brisbane/Singapore/Toronto: John Wiley and Sons, INC: 1-656.

Liu, X., Liu, X. & Hu, Y. 2014. Investigation of the thermal decomposition of talc. *Clays and Clay Minerals*, 62:137–144.

Manuppella, C., Antunes, T. M., Almeida, C. C. A., Azerêdo, A. C., Barbosa, B., Cardoso, J. L., Crispim, J. A., Duarte, L. V., Henrique, M. H., Martins, L. T., Ramalho, M. M., Santos, V. F. & Terrinha, P. 2000. Notícia explicativa da Carta Geológica de Portugal à escala 1:50 000, folha 27-A (Vila Nova de Ourém). *Departamento de Geologia. Instituto Geológico e Mineiro:* 1:1-67.

Mateus, J. E. & Fernanda Queiroz, P. 2012. *A Gruta-Povoado da AVECASTA Uma introdução ilustrada ao sítio arqueológico e ao seu programa de estudo e valorização*. *Terra Scenica.* 1:1-70.

Moreira, N., Romão, J., Dias, Pedro. R. & Ribeiro A. 2016. The Porto-Tomar- Ferreira do Alentejo Shear Zone tectonostratigraphy in Tomar-Abrantes sector (Portugal). *Geo-Temas*, 16: 85–88.

Navarrete Enciso, M. S. 1976. La cultura de las cuevas con ceramica decorada en andalucia oriental*, Articulos,* 1:59-73.

Oosterbeek, L. 1993. Nossa Senhora das Capas: excavation of pre-historic cave burial in central Portugal. *Papers from the Institute of Archaeology*, 4:49–62.

Perrin, C., Prestimonaco, L., Servelle, G., Tilhac, R., Maury, M. & Cabrol, P. 2014. Aragonite-Calcite Speleothems: Identifying Original and Diagenetic Features. *Journal of Sedimentary Research*, 84: 245–269.

Quinn, P. S. 2013. *Ceramic petrography the interpretation of archaeological pottery & related artefacts in thin section*. England, Archaeopress: 1-251.

Romão, J. 2006. Notícia explicativa da Carta Geológica de Portugal à escala 1:50 000, folha 28-A, Mação. *Departamento de Geologia. Instituto Nacional de Engenharia, Tecnologia e Inovação*, 1:1-77

Riccardi, M. P., Messiga, B. & Duminuco, P. (1999). An approach to the dynamics of clay firing. *Applied Clay Science* 15: 393-409.

Rice, M. P. 2005. *Pottery Analysis*. Chicago, US, The University of Chicago Press, Ltd.:1–394.

Sitzia, F., Beltrame, M. & Mirão, J., 2022. The particle-size distribution of concrete and mortar aggregates by image analysis. *Journal of Building Pathology and Rehabilitation*, 7(1). https://doi.org/10.1007/s41024-022-00214-w.

Soares, F. A., Marques, J. F. & Sequeira, A. J. D. 2007. Notícia explicativa da Carta Geológica de Portugal à escala 1:50 000, folha 19-D (Coimbra - Lousã). *Serviço Geológico de Portugal. Direção Geral de Minas e Serviços Geológicos*, 1:1-22.

Stojanovski, D., Roffet-Salque, M., Casanova, E., Knowles, T., Oosterbeek, L., Evershed, R. P., Cruz, A., Thissen, L. & Arzarello, M. 2020. Anta 1 de Val da Laje – the first direct view of diet, dairying practice and socio-economic aspects of pottery use in the final Neolithic of central Portugal. *Quaternary International*, 542:1–8.

Teixeira, C., Zbyszewski, G., Torre de Assunção, C. & Manupella, G. 1968. Notícia explicativa da Carta Geológica de Portugal à escala 1:50 000, folha 23-C (Leiria). *Departamento de Geologia. Instituto Nacional de Engenharia, Tecnologia e inovação.* 1: 1-90.

Veizer, J. 1978. Simulation of limestone diagenesis—a model based on strontium depletion: Discussion. *Canadian Journal of Earth Sciences*, 15:1683–1685.

Velde, B., & Druc, I. C. 1999. *Archaeological Ceramic Materials*. Berlin Heidelberg, Springer Press, 1-312.

Zilhão, J. 1988. Plaquette gravée du Solutréen supérieur de la Gruta do Caldeirão (Tomar, Portugal). *Bulletin de La Société Préhistorique Française*, 85: 105–109.

ANNEXES

Annex. 1. Fabric data including minerals and rock fragments identified. Plagioclase (Pla), quartz (Q), potassium feldspar (Kf), biotite (Bio), muscovite (Mu), Amp: Amphibole, Calcite (Cal), oxides (Ox).

Sample No.	Samples Arc. Ref.	Fabric	Mineralogy	Rock fragments	Observations
AVE_S1	P28-211	1	Ca, Q	Limestone	Thermally altered calcite
AVE_S2	P28-166	2	Q, Bio, Mu, Pla	Schist rich in biotite, Quartzite	Rich in Quartzite and biotite
AVE_S3	R27-90	2	Q, Kf, Mu, Pla	Schist rich in biotite, Quartzite	Rich in Quartzite, biotite, and grog
AVE_S4	R27-87	3	Q, Kf, Mu	Limestone, sandstone	
AVE_S5	R28-528	4	Q, Pla, Kf, Mu	Granitic rock, schist rich in muscovite, quartzite	Has muscovite with grog
AVE_S6	R28-512	3	Ca, Q, Pla, Mu	Limestone, Quartzite	
AVE_S7	R27-465	2	Q, Mu, Bio, Pla, Kf	Granitic rock, schist rich in biotite, quartzite	Rich in biotite
AVE_S8	P28-168	1	Ca, Q, Pla, Kf	Limestone, Quartzite	Thermally altered calcite
AVE_S9	R27-462	2	Q, Bio, mu Amp	Biotite schist, Granitic rock, and sandstone	Rich in biotite
AVE_S10	R27-478	1	Ca, Q	Limestone	Thermally altered calcite
AVE_S11	R27-463	2	Q, Mu, Bio, Pla, Kf, Amp	Granitic rock, Quartzite	Rich in Biotite
AVE_S12	R27-601	2	Q, Mu, Kf, Bio, Amp		Rich in Biotite
AVE_S13	R28-540	3	Ca, Q, Mu	Limestone, Marble?	
AVE_S14	P27-604	2	Q, Mu, Bio, Pla, Kf, Amp	Sandstone, Quartzite, Granitic rock	Rich in quartzite, and biotite
AVE_S15	Q28-579	1	Ca, Q	Limestone, Marble?	
AVE_S16	R28-609	2	Q, Bio, Pla, Kf, Amp	Biotite rich schist, and Granitic rock	Rich biotite and grog
AVE_S17	Q28-567	3	Q, Mu, Pla, Kf	Limestone, Schist rich in muscovite, Quartzite	
AVE_S18	R28-570	1	Ca, Q	Limestone	
AVE_S19	R27-507	4	Q, Mu, Bio, Pla, Mu	Granitic rock,schist rich in muscovite Quartzite	Possesses muscovite with grog
AVE_S20	P28-526	1	Ca, Q	Marble?	
AVE_S21	Q28-553	4	Q, Mu, Bio, Pla, Kf, Amp	Muscovite rich schist, sandstone, Quartzite, Granitic rock	Rich in Muscovite
AVE_S22	R28-606	2	Q, Mu, Buo, Pla, Kf, Amp	Granitic rock, Muscovite rich schist	With muscovite and grog
AVE_S23	R27-510	2	Q, Mu, Bio, Pla, Kf, Amp	Biotite rich schist, and Granitic rock	Lime pellets, rich in biotite
AVE_S24	R27-581	1	Q, Ca	Limestone, Marble?	
AVE_S25	P28-578	1	Q, Ca	Limestone, Marble?	
AVE_S26	R28-604	4	Q, Mu, Pla, Kf	Quartzite, Sandstone, Schist rich in muscovite	Has muscovite with grog
AVE_S27	P28-620	4	Q, Mu, Pla, Kf, Bio	Granitic rock, Schist rich in muscovite Quartzite	Rich in Muscovite
AVE_S28	P28-703	1	Q, Ca	Marble?, Quartzite	
AVE_S29	P28-623	1	Q, Ca	Limestone Marble?, Quartzite	Thermally altered calcite
AVE_S30	Q28-727	1	Q, Ca	Marble??	
AVE_S31	Q28-726	1	Q, Ca	Marble??	
AVE_S32	Q28-713	1	Q, Ca	Marble??	
AVE_S33	R28-850	1	Q, Ca	Limestone, Marble?? Quartzite	Thermally altered calcite
AVE_S34	P28-806	1	Q, Ca	Marble?	
AVE_S35	Q28-877	3	Q, Mu, Pla. Kf	Limestone, Calcarenite	
AVE_S36	R28-825	1	Q, Kf, Ca	Marble?	
AVE_S37	P28-780	1	Q, Mu, Ca	Limestone, Marble?	Thermally altered limestone
AVE_S38	Q27-156	3	Q, Mu, Kf	Limestone, Marble?, Quartzite	
AVE_S39	P27-161	4	Q, Mu, Bio, Pla, Kf	Biotite schist, Granitic rocks, Quartzite, small amount of Limestone	Rich in muscovite
AVE_S40	P27-201	4	Q, Mu, Bio, Pla, Kf	Quartzite, schist rich in muscovite,	Has muscovite with grogs
AVE_S41	P27-106	4	Q, Mu, Bio, Pla, Kf	Granitic rock, schist rich in biotite, Quartzite	It has muscovite
AVE_S42	R27-207	3	Q, Mu, Ca, Pla, Kf	Limestone	

Annex. 2. Petrographic data. Showing sample reference number, chronology, and other petrographic data such as: Matrix homogeneity/heterogeneity: H.HOM., highly homogeneous – M.HOM., moderately homogeneous – S.HOM., slightly homogeneous – H.HET., highly heterogeneous – M.HET., moderately heterogeneous -S.HET., slightly heterogeneous. Fe-Ca rich matrix: Fe, iron rich matrix -Ca rich matrix, Matrix activity: S, slightly active – M, moderately active – H, highly active – I, isotropic. Alignment: W, weak – M, moderate, main grain shape: Eq&El, mainly equal (rounded) and elongated grains – El&Eq, mainly elongated and equal grains. Roundness: VA, very angular – A, angular -SA, sub-angular – SR. sub-rounded – R, rounded – WR, well rounded. Packing: CS, closed spaced – SS, single spaced – DS, double spaced -OS, open spaced. Sorting: VP, very poor – P, poor – M, moderate – W, Well. Grain Size Distribution (GSD.): U, unimodal -B, bimodal.

Sample n.	*Samples Arc. Ref.*	*Fabric*	*Ceramic paste*					*Porosity*	*Temper*							
			Colour	*Hom. – Het.*	*Fe- Ca rich matrix*	*Activity*	*Oxides*	*Description*	*Shape*	*Roundness*	*Packing*	*Max size µm*	*Alignment*	*Sorting*	*G.S.D.*	*%*
AVE_S1	P28-211	1	Brown	S.HET	Fe	S	X	Micro.meso vesicles,and meso-macro elongated voids	Eq&El	A-SR	CS	3.15mm	P	P	U	17.13
AVE_S2	P28-166	2	Brown	M.HOM	Fe	S	X	Micro.meso vesicles, and vughs	El&Eq	SR-R	SS	5.48mm	P	P	B	16.17
AVE_S3	R27-90	2	Brown	S.HET	Fe	S	X	Meso vesicles, and meso elongated voids	Eq	SA-R	SS	1.13mm	P	M	U	4.73
AVE_S4	R27-87	3	Brown	S.HET	Fe	M	X	Micro-Meso vesicles	Eq&El	SA-R	CS	1.58mm	P	M	U	20.52
AVE_S5	R28-528	4	Brown	M.HOM	Fe	S	X	Micro.meso vesicles, and vughs	Eq&El	SA-R	SS	1.56mm	P	P	B	15.21
AVE_S6	R28-512	3	Brown	M.HET	Fe	S	X	Meso vesicles and macro elongated voids	Eq&El	SR-R	SS	1,31mm	P	P	B	8.91
AVE_S7	R27-465	2	Brown	M.HOM	Fe	S	X	Meso vesicles, and Meso Elongated voids	Eq	SA-R	CS	2.46mm	P	M	B	27.80
AVE_S8	P28-168	1	Brown	S.HOM	Fe	S	X	Micro.meso vesicles and elongated voids	Eq&El	A-SA	CS	2,01mm	P	M	U	22.04
AVE_S9	R27-462	2	Brown	M.HOM	Fe	M	X	Micro vesicles and Meso elongated voids	Eq&El	SA-R	SS	1.07mm	P	P	B	21.16
AVE_S10	R27-478	1	Brown	M.HOM	Fe	I	X	Micro.meso vesicles, and meso elongated voids	El &Eq	A-SR	SS	2.33mm	P	P	U	23.81
AVE_S11	R27-463	2	Brown	M.HOM	Fe	S	X	Micro-meso vesicles	Eq&El	SA-R	CS	2.35mm	P	M	B	10.96
AVE_S12	R27-601	2	Brown	M.HOM	Fe	S	X	Micro.meso vesicles, channels, and vughs	Eq&El	SR-R	SS	0.58mm	P	M	B	12.18
AVE_S13	R28-540	3	Brown	M.HOM	Fe	M	X	Meso vesicles, meso elongated voids and vughs	Eq	SA-R	DS	1.08mm	P	P	B	17.79
AVE_S14	P27-604	2	Brown	M.HOM	Fe	S	X	Meso vesicles, and meso elongated voids	Eq&El	SA-R	CS	1.57mm	P	P	U	27.59
AVE_S15	Q28-579	1	Brown	M.HOM	Fe	S	X	Micro.meso vesicles, and meso elongated voids	Eq&El	A-SR	SS	2.04mm	P	P	U	19.21
AVE_S16	R28-609	2	Brown	S.HET.	Fe	S	X	Meso vesicles and Meso	Eq&El	SA-R	DS	1.04mm	P	M	B	5-10

Sample n.	Samples Arc. Ref.	Fabric	Ceramic paste					Porosity	Temper							
			Colour	Hom. – Het.	Fe- Ca rich matrix	Activity	Oxides	Description	Shape	Roundness	Packing	Max size µm	Alignment	Sorting	G.S.D.	%
								elongated voids								
AVE_S17	Q28-567	1	Brown	S.HET	Fe	S	X	Micro.meso vesicles, meso elongated voids and neso vughs	Eq&El	A-R	OS	1.10mm	P	B	P	11.48
AVE_S18	R28-570	1	Brown	M.HET	Fe	S	X	Micro.meso vesicles, micro-meso elongated voids and meso vughs	Eq&El	A-SR	SS	1.77mm	P	P	B	28.26
AVE_S19	R27-507	4	Brown	M.HOM	Fe	S	X	Meso vesicles, and meso elongated voids	Eq	SA-R	DS	0.93mm	P	P	B	7.51
AVE_S20	P28-526	1	Brown	M.HOM	Fe	S	X	Micro.meso vesicles, and meso elongated voids	Eq&El	SA-R	SS	2.00mm	P	P	U	28.81
AVE_S21	Q28-553	4	Brown	M.HOM	Fe	S	X	Micro.meso vesicles, and vughs	Eq&EL	SA-R	SS	1.93mm	P	P	B	10.20
AVE_S22	Q28-606	2	Dark brown	S.HET.	Fe	S	X	Micro.meso vesicles, and meso elongated voids	Eq	SR-R	DS	1.23mm	P	W	B	9.12
AVE_S23	R27-510	2	Brown	S.HET	Fe	S	X	Micro.meso vesicles, and vughs	Eq&El	SA-R	SS	2.76mm	P	M	U	16.01
AVE_S24	R27-581	1	Brown	M. HOM	Fe	S	X	Micro-meso vesicles, meso-mega elongated voids	Eq&El	A-SR	SS	1.93mm	P	P	U	21.70
AVE_S25	P28-578	1	Brown	S.HET	Fe	S	X	Micro.meso vesicles and meso elongated voids	Eq&El	SA-R	SS	3,44mm	P	P	U	27.24
AVE_S26	R28-604	4	Buffy red	S.HOM.	Fe	M	X	meso vesicles, micro elongated voids, and meso vughs	El&Eq	SA-R	SS	2.22mm	P	P	B	13.54
AVE_S27	P28-620	4	Brown	M.HOM	Fe	M	X	Micro.meso vesicles, and vughs	Eq&El	SA-SR	CS	1.88mm	P	P	B	25.30
AVE_S28	P28-703	1	Brown	M.HOM	Fe	S	X	Micro.meso vesicles and micro and meso elongated voids	Eq&El	A-SA	CS	1.84mm	P	P	U	23.29
AVE_S29	P28-623	1	Brown	S.HET	Fe	I	X	Micro.meso vesicles, and meso elongated voids	El&Eq	SA-R	CS	2.00mm	M	P	B	26.42
AVE_S30	Q28-727	1	Brown	S.HET	Fe	S	X	Micro.meso vesicles and meso elongated voids	Eq&El	SA-SR	CS	1.26mm	P	P	U	25.57
AVE_S31	Q28-	1	Brown	S.HET	Fe	S	X	meso	Eq&El	SA-	CS	1.07mm	M	P	U	25.57

Sample n.	Samples Arc. Ref.	Fabric	Ceramic paste					Porosity	Temper							
			Colour	Hom. – Het.	Fe- Ca rich matrix	Activity	Oxides	Description	Shape	Roundness	Packing	Max size µm	Alignment	Sorting	G.S.D.	%
	726							elongated voids and meso vughs		R						
AVE_S32	Q28-713	1	Brown	H-Hom	Fe	S	X	Micro-meso vesicles and meso-elongated voids	Eq&El	A-SR	Cs	2.85mm	P	P	U	20.14
AVE_S33	R28-850	1	Brown	M.HOM	Fe	S	X	Micro.meso vesicles and meso elongated voids	Eq&El	A-R	CS	1.94mm	M	P	U	28.00
AVE_S34	P28-806	1	Brown	S.HET	Fe	S	X	Micro.-meso vesicles, and meso elongated voids	Eq&El	SA-SR	SS	2.15mm	M	P	B	21.73
AVE_S35	Q28-877	3	Brown	S.HET	Fe	S	X	Macro elongated voids	Eq	SA-R	SS	2,51mm	P	P	U	24.07
AVE_S36	Q28-825	1	Brown	M.HOM	Fe	S	X	Micro.meso vesicles, and meso elongated voids	Eq&El	SA-R	CS	2.18mm	P	P	B	25.27
AVE_S37	P28-780	1	Brown	M.HOM	Fe	S	X	Micro.meso vesicles and meso.macro elongated voids	Eq&El	SA-R	SS	2.52mm	P	P	B	21.86
AVE_S38	*Q27-156*	3	Dark brown	S.HET	Fe	S	X	Micro-meso vesicles and meso elongated voids	Eq	SA-R	SS	3.60mm	P	P	B	22.17
AVE_S39	P27-161	4	Dark brown	M.HOM	Fe	I	X	Micro.meso vesicles, and meso elongated voids	Eq&El	SA-R	DS	1.00mm	P	M	B	20.30
AVE_S40	P27-201	4	Brown	M.HOM	Fe	S	X	Micro.meso vesicles, and vughs	Eq&El	SA-R	SS	1.65mm	P	P	B	27.50
AVE_S41	P27-106	4	Dark brown	M.HOM	Fe	S	X	Meso vesicles and macro elongated voids	Eq&El	SA-R	DS	1.38mm	P	P	B	23.30
AVE_S42	R27-207	3	Brown	S.HET	Fe	S	X	Micro-meso vesicles and meso elongated voids	Eq&El	SA-R	OS	3.63mm	P	P	B	7.83

Annex. 3. XRF data – Major oxides and loss on ignition (LOI) of all the forty-two samples.

Sample No.	Samples Arc. Ref.	Concentration/St.Error	Na_2O	MgO	Al_2O_3	SiO_2	P_2O_5	K_2O	CaO	TiO_2	Fe_2O_3	LOI
AVE S1	P28-211	wt.%	0.01	0.51	18.37	26.96	1.37	0.8	25.59	0.79	1.24	25.82
		Stat Error ± (%)	± 0,00474	± 0,00228	± 0,00364	± 0,00231	± 0,000380	± 0,00284	±0,00748	± 0,000939	± 0,000353	
AVE S2	P28-166	wt.%	1.27	1.6	16.26	65.21	0.25	4	0.94	0.57	4.94	5.39
		Stat Error ± (%)	± 0,00551	± 0,00252	± 0,00336	± 0,00350	- ± 0,000222	± 0,00428	±0,00210	± 0,000880	± 0,000720	
AVE_S3	R27-90	wt.%	0.26	3.91	19.64	57.51	0.26	4.19	2.18	0.87	7.32	3.51
		Stat Error ± (%)	± 0,00503	± 0,00311	± 0,00369	± 0,00350	± 0,000238	± 0,00425	±0,00277	± 0,000995	± 0,000829	
AVE_S4	R27-87	wt.%	1.29	0.49	23.07	46.26	0.77	1.51	8.1	0.94	4.46	13.39
		Stat Error ± (%)	± 0,00559	± 0,00224	± 0,00404	± 0,00299	± 0,000306	± 0,00326	±0,00452	± 0,00104	± 0,000683	
AVE S5	R28-528	wt.%	1.14	3.65	17.74	57.57	0.51	5.14	1.95	0.74	6.7	6.11
		Stat Error ± (%)	± 0,00533	± 0,00352	± 0,00332	± 0,00309	± 0,000262	± 0,00472	±0,00247	± 0,000946	± 0,000802	
AVE S6	R28-512	wt.%	0.61	1.02	22.59	54.6	0.32	1.66	6.61	0.88	4.39	7.03
		Stat Error ± (%)	± 0,00516	± 0,00238	± 0,00396	± 0,00322	± 0,000238	± 0,00329	±0,00411	± 0,00101	± 0,000673	
AVE S7	R27-465	wt.%	1.6	2.37	18.92	60.76	0.36	2.51	1.54	0.75	6.77	4.52
		Stat Error ± (%)	± 0,00582	± 0,00278	± 0,00368	± 0,00344	± 0,000247	± 0,00371	±0,00239	± 0,000968	± 0,000844	
AVE S8	P28-168	wt.%	0.09	0.47	13.9	23.72	0.61	0.55	30.58	0.68	1.81	28.6
		Stat Error ± (%)	± 0,00463	± 0,00259	± 0,00302	± 0,00203	± 0,000287	± 0,00276	±0,00785	± 0,000885	± 0,000410	
AVE S9	R27-462	wt.%	1.18	2.62	19.48	53.35	0.23	1.73	1.37	1.89	10.28	8.56
		Stat Error ± (%)	± 0,00550	± 0,00334	± 0,00358	± 0,00307	± 0,000225	± 0,00344	±0,00222	± 0,00135	± 0,00100	
AVE S10	R27-478	wt.%	0.28	0.57	10.92	22.69	0.45	0.48	33.53	0.56	4.1	27.58
		Stat Error ± (%)	± 0,00500	± 0,00273	± 0,00278	± 0,00205	± 0,000273	± 0,00263	±0,00811	± 0,000815	± 0,000606	
AVE S11	R27-463	wt.%	1.54	4.05	21.05	53.02	0.09	2.01	0.88	2.09	12.58	1.47
		Stat Error ± (%)	± 0,00623	± 0,00331	± 0,00401	± 0,00353	± 0,000215	± 0,00341	±0,00211	± 0,00139	± 0,00109	
AVE S12	R27-601	wt.%	0.37	3.66	17.44	58.24	0.35	4.75	0.95	0.78	7.07	6.28
		Stat Error ± (%)	± 0,00506	± 0,00304	± 0,00347	± 0,00351	± 0,000251	± 0,00437	±0,00210	± 0,000921	± 0,000806	
AVE S13	R28-540	wt.%	0.16	0.57	21.74	50.73	0.72	1.29	7.99	1.53	7.33	7.74
		Stat Error ± (%)	± 0,00438	± 0,00202	± 0,00255	± 0,00213	± 0,000237	± 0,00293	±0,00352	± 0,000965	± 0,000591	
AVE S14	P27-604	wt.%	0.93	1.75	15.24	60.58	0.41	2.01	2.06	1.57	8.54	7.98
		Stat Error ± (%)	± 0,00549	± 0,00267	± 0,00342	± 0,00353	± 0,000261	± 0,00349	±0,00263	± 0,00126	± 0,000945	

AVE S15	Q28-579	wt.%	0.1	1.49	13.21	31.58	0.65	0.61	23.36	0.81	3.31	25.41
		Stat Error ± (%)	± 0,00480	± 0,00259	± 0,00320	± 0,00256	± 0,000302	± 0,00274	±0,00722	± 0,000960	± 0,000575	
AVE S16	R28-609	wt.%	0.8	3.52	18.57	57.75	0.35	4.28	1.53	0.83	7.03	5.5
		Stat Error ± (%)	± 0,00514	± 0,00347	± 0,00339	± 0,00309	± 0,000237	± 0,00447	±0,00230	± 0,000991	± 0,000826	
AVE S17	Q28-567	wt.%	0.42	0.52	21.25	49.39	0.78	1.51	5.59	1.32	7.23	11.92
		Stat Error ± (%)	± 0,00485	± 0,00260	± 0,00366	± 0,00289	± 0,000305	± 0,00332	±0,00370	± 0,00116	± 0,000838	
AVE S18	R28-570	wt.%	0.03	0.66	12	23.82	0.4	0.71	34.63	0.57	2.01	27.14
		Stat Error ± (%)	± 0,00455	± 0,00214	± 0,00239	± 0,00183	± 0,000236	± 0,00272	±0,00762	± 0,000767	± 0,000360	
AVE S19	R27-507	wt.%	0.51	0.6	19.17	61.7	0.34	1.66	1.71	1.09	3.9	9.6
		Stat Error ± (%)	± 0,00467	± 0,00248	± 0,00331	± 0,00307	± 0,000229	± 0,00345	±0,00241	± 0,00110	± 0,000624	
AVE S20	P28-526	wt.%	0.35	0.5	16.39	35.33	0.54	0.86	21.01	0.82	4.06	20.71
		Stat Error ± (%)	± 0,00512	± 0,00232	± 0,00352	± 0,00269	± 0,000284	± 0,00285	±0,00682	± 0,000958	± 0,000634	
AVE S21	Q28-553	wt.%	0.72	2.05	19.82	59.97	0.27	4.04	0.97	0.37	7.92	3.9
		Stat Error ± (%)	± 0,00530	± 0,00272	± 0,00383	± 0,00347	± 0,000233	± 0,00427	±0,00210	± 0,000785	± 0,000907	
AVE S22	Q28-606	wt.%	0.29	3.32	20.27	58.51	0.25	4.15	1.71	0.92	7.65	1.92
		Stat Error ± (%)	± 0,00505	± 0,00300	± 0,00376	± 0,00355	± 0,000238	± 0,00424	±0,00255	± 0,00101	± 0,000844	
AVE S23	R27-510	wt.%	1.33	2.43	18.08	52.01	0.68	1.73	1.93	1.73	9.34	9.72
		Stat Error ± (%)	± 0,00604	± 0,00329	± 0,00279	± 0,00281	± 0,000316	± 0,00405	±0,00201	± 0,00105	± 0,00108	
AVE S24	R27-581	wt.%	0.13	1.23	14.98	30.49	0.51	1.82	23.39	0.7	3.95	22.72
		Stat Error ± (%)	± 0,00468	± 0,00287	± 0,00313	± 0,00231	± 0,000272	± 0,00338	±0,00692	± 0,00089	± 0,000604	
AVE S25	P28-578	wt.%	0.46	0.73	12.62	29.62	0.37	0.69	26.52	0.82	2.28	26.96
		Stat Error ± (%)	± 0,00493	± 0,00269	± 0,00287	± 0,00226	± 0,000249	± 0,00281	±0,00734	± 0,000958	± 0,000460	
AVE S26	R28-604	wt.%	0.33	1.85	19.35	54.85	0.49	4.02	1.91	0.96	7.59	7.98
		Stat Error ± (%)	± 0,00477	± 0,00302	± 0,00348	± 0,00303	± 0,000262	± 0,00437	±0,00247	± 0,00104	± 0,000859	
AVE S27	P28-620	wt.%	1.52	1.42	12.79	64.41	0.56	2.43	2.1	0.61	7.75	6.6
		Stat Error ± (%)	± 0,00588	± 0,00257	± 0,00313	± 0,00362	± 0,000281	± 0,00367	±0,00265	± 0,000907	± 0,000902	
AVE S28	P28-703	wt.%	0.29	1.24	12.23	41.94	0.82	1.99	18.02	0.47	5.16	17.66
		Stat Error ± (%)	± 0,00477	± 0,00287	± 0,00284	± 0,00269	± 0,000314	± 0,00349	±0,00615	± 0,000811	± 0,000694	
AVE S29	P28-623	wt.%	0.36	0.69	15.01	28.66	0.44	0.77	25.48	0.68	3.68	24.37
		Stat Error ± (%)	± 0,00493	± 0,00270	± 0,00315	± 0,00225	± 0,000263	± 0,00288	±0,00723	± 0,000899	± 0,000585	
AVE S30	Q28-727	wt.%	0.06	4.08	10.73	28.67	0.84	2.87	26.73	0.4	3.63	24.98

		Stat Error ± (%)	± 0,00467	± 0,00298	± 0,00253	± 0,00211	± 0,000295	± 0,00356	±0,00691	± 0,000742	± 0,000538	
AVES31	Q28-726	wt.%	0.29	3.9	10.61	28.39	0.69	2.8	25.11	0.38	3.33	24.46
		Stat Error ± (%)	± 0,00493	± 0,00368	± 0,00268	± 0,00224	± 0,000300	± 0,00377	±0,00713	± 0,000751	± 0,000553	
AVES32	Q28-713	wt.%	0.08	0.76	15.37	29.02	0.5	1.29	25.24	0.72	2.64	24.15
		Stat Error ± (%)	± 0,00459	± 0,00269	± 0,00315	± 0,00223	± 0,000270	± 0,00316	±0,00719	± 0,000911	± 0,000496	
AVES33	R28-850	wt.%	0.19	1.13	11.21	35.6	0.51	1.77	23.49	0.6	4.11	22.42
		Stat Error ± (%)	± 0,00502	± 0,00252	± 0,00297	± 0,00272	± 0,000284	± 0,00329	±0,00717	± 0,000889	± 0,000634	
AVES34	P28-806	wt.%	0.04	0.59	16.89	37.26	0.61	0.78	17.94	0.9	4.85	21.85
		Stat Error ± (%)	± 0,00464	± 0,00218	± 0,00304	± 0,00249	± 0,000276	± 0,00283	±0,00611	± 0,000947	± 0,000609	
AVES35	Q28-877	wt.%	0.25	0.5	16.46	41.22	0.46	1.37	17.15	0.73	4.35	17.96
		Stat Error ± (%)	± 0,00498	± 0,00230	± 0,00352	± 0,00289	± 0,000271	± 0,00311	±0,00624	± 0,000928	± 0,000660	
AVES36	R28-825	wt.%	0.11	1.13	10.77	37.14	0.43	1.78	22.56	0.42	4.12	21.93
		Stat Error ± (%)	± 0,00491	± 0,00250	± 0,00292	± 0,00279	± 0,000268	± 0,00327	±0,00706	± 0,000771	± 0,000638	
AVES37	P28-780	wt.%	0.38	0.7	12.78	25.37	0.43	0.77	29.98	0.55	2.14	28.81
		Stat Error ± (%)	± 0,00510	± 0,00236	± 0,00313	± 0,00229	± 0,000269	± 0,00281	±0,00803	± 0,000841	± 0,000459	
AVES38	Q27-156	wt.%	0.52	0.71	24.09	50.77	0.43	1.3	3.54	1.3	7.6	8.96
		Stat Error ± (%)	± 0,00514	± 0,00235	± 0,00422	± 0,00321	± 0,000263	± 0,00317	±0,00320	± 0,00117	± 0,000891	
AVES39	P27-161	wt.%	1.53	0.9	18.88	63.17	0.34	1.83	2.49	0.37	4.35	9.63
		Stat Error ± (%)	± 0,00563	± 0,00232	± 0,00359	± 0,00342	± 0,000235	± 0,00345	±0,00283	± 0,000792	± 0,000680	
AVES40	P27-106	wt.%	0.41	0.85	16.22	62.6	2.54	2.47	2.14	0.53	5.52	6.27
		Stat Error ± (%)	± 0,00477	± 0,00264	± 0,00312	± 0,00316	± 0,000461	± 0,00378	±0,00256	± 0,000866	± 0,000736	
AVES41	P27-201	wt.%	1.35	0.81	18.11	63.34	0.26	2.13	0.85	0.71	7.73	4.36
		Stat Error ± (%)	± 0,00569	± 0,00237	± 0,00366	± 0,00356	± 0,000232	± 0,00356	±0,00204	± 0,000951	± 0,000904	
AVES42	R27-207	wt.%	0.29	0.61	20.76	49.51	0.55	1.2	8.1	1.11	7.23	12.53
		Stat Error ± (%)	± 0,00500	± 0,00232	± 0,00395	± 0,00318	± 0,000283	± 0,00307	±0,00448	± 0,00109	± 0,000861	

Annex. 4. XRF data of trace elemental concentration and statistical error (ppm) of the samples.

Sample No.	Sample Arc. Ref.	Concentration/Sta. Error	Rb	Sr	Y	Zr	Nb	Ba	Th	Cr	Ni	Cu	Zn	Ga	As	Pb	V	U	Mn
AVES1	P28-211	ppm	17.44	69.69	15.33	174.53	18.91	733.05	3.91	85.88	36.6	24.72	76.38	18.6		17.03	109.44		120.59
		Stat,Er±(%)	±0,338	±0,45	±0,10	±0,44	±0,28	±2,49	±0,325	±0,650	±0,396	±0,279	±0,371	±0,0955		±1,41	±1,59		±0,784
AVES2	P28-166	ppm	126.63	86.55	25.27	199.4	9.77	779.61	9.19	30.67	22.29	29.31	70.22	19.89		30.52	104.95		296.31
		Stat,Er±(%)	±0,38	±0,490	±0,11	±0,477	±0,307	±2,49	±0,349	±0,680	±0,406	±0,299	±0,386	±0,102		±1,51	±1,61		±0,916
AVE_S3	R27-90	ppm	151.59	92.98	42.77	194.51	17.15	842.75	16.19	150.48	75.98	30.91	140.6	23.53		45.91	96.94	0.9	1027.83
		Stat,Er±(%)	±0,366	±0,43	±0,118	±0,563	±0,312	±2,51	±0,335	±0,735	±0,537	±0,297	±0,392	±0,101		±1,30	±1,72	±0,180	±1,10
AVE_S4	R27-87	ppm	79	69.97	24.86	248.88	20.24	665.32	14.31	100.96	31.17	28.05	48.89	28.45	4.95	19.21	122.96	2.7	367.4
		Stat,Er±(%)	±0,370	±0,479	±0,114	±0,477	±0,302	±2,46	±0,343	±0,699	±0,417	±0,297	±0,359	±0,103	±1,41	±1,48	±1,72	±0,198	±0,927
AVES5	R28-528	ppm	182.08	75.96	45.42	181.37	25.12	650.83	13.09	88.44	50.78	35.17	173.53	21.32		59.27	166.21	7.79	1681.15
		Stat,Er±(%)	±0,384	±0,448	±0,117	±0,622	±0,308	±2,44	±0,332	±0,706	±0,491	±0,298	±0,424	±0,100		±1,24	±1,70	±0,186	±1,24
AVES6	R28-512	ppm	78.82	121.76	30.39	207.33	23.77	588.17	12.64	102.7	49.12	48.01	71.94	27.26		31.48	124.78	2.19	329.73
		Stat,Er±(%)	±0,369	±0,488	±0,114	±0,470	±0,302	±2,44	±0,343	±0,694	±0,432	±0,312	±0,385	±0,102		±1,49	±1,69	±0,197	±0,904
AVES7	R27-465	ppm	119.15	239.36	30.81	463.21	19.4	1018.41	17.17	163.46	106.04	21.13	115.01	22.14	0.51	24.9	82.83	5.38	368.5
		Stat,Er±(%)	±0,381	±0,515	±0,115	±0,515	±0,303	±2,51	±0,346	±0,752	±0,507	±0,298	±0,433	±0,102	±1,38	±1,49	±1,69	±0,199	±0,963
AVES8	P28-168	**ppm**	21.27	62.73	25.7	176.61	15.97	736.54	8.35	79.23	56.68	14.9	29.39	13.02	11.73	24.27	113.85	4.39	96.74
		Stat,Er±(%)	±0,328	±0,420	±0,109	±0,588	±0,291	±2,46	±0,311	±0,634	±0,462	±0,267	±0,291	±0,0920	±1,48	±1,15	±1,53	±0,174	±0,762
AVES9	R27-462	ppm	58.99	138.55	22.81	184.84	19.52	954.45	12.64	109.39	89.18	33.16	127.88	18.66		48.4	163.05	3.33	797.37
		Stat,Er±(%)	±0,315	±0,404	±0,104	±0,568	±0,279	±2,38	±0,300	±0,624	±0,417	±0,257	±0,259	±0,0881	±1,46	±1,11	±1,46		±0,836
AVES10	R27-478	ppm	16.39	60.69	16.32	180.34	14.28	500.77	6.35	56.24	25.57	18.61	13.37	11.97	10.16	20.23	92.73		313.22
		Stat,Er±(%)	±0,315	±0,404	±0,104	±0,568	±0,279	±2,38	±0,300	±0,624	±0,417	±0,257	±0,259	±0,0881	±1,46	±1,11	±1,46		±0,836
AVES11	R27-463	ppm	74.33	251.48	24.31	286.59	41.16	796.06	20.05	288.07	166.33	22.82	74.37	22.19	3.62	2.65	210.38		786.46
		Stat,Er±(%)	±0,340	±0,455	±0,113	±0,570	±0,305	±2,45	±0,325	±0,814	±0,654	±0,289	±0,337	±0,0984	±1,45	±1,25	±2,12		±1,08
AVES12	R27-601	ppm	183.39	68.65	44.42	192.85	26.63	244.35	25.95	152.77	152.26	52.92	188.01	22.09	15.53	42.06	159.02	6.85	1201.7

		Stat,Er±(%)	±0,370	±0,431	±0,117	±0,557	±0,310	±2,34	±0,335	±0,713	±0,617	±0,314	±0,425	±0,0999	±1,41	±1,30	±1,63	±0,180	±1,13
AVE S13	R28-540	ppm	72.78	130.99	60.65	447.07	61.03	735.21	44.66	218.43	103.9	58.47	75.29	36.17	6.1	85.98	280.95	15.92	951.25
		Stat,Er±(%)	±0,394	±0,498	±0,134	±0,642	±0,359	±2,46	±0,389	±0,736	±0,534	±0,310	±0,325	±0,109	±1,43	±1,51	±1,70	±0,210	±0,987
AVE S14	P27-604	ppm	71.27	92.59	29.02	238.18	18.12	773.22	15.06	195.96	37.84	31	91.17	19.35	4.34	59.94	203.92	1.43	2498.32
		Stat,Er±(%)	±0,362	±0,475	±0,112	±0,468	±0,296	±2,47	±0,338	±0,758	±0,434	±0,299	±0,402	±0,0988	±1,39	±1,47	±1,98	±0,194	±1,40
AVE S15	Q28-579	ppm	17.98	47.52	15.37	205.55	18.48	780.79	0.67	60.75	19.18	26.14	47.75	15.94	3.66	24.5	90.72	0.84	334.11
		Stat,Er±(%)	±0,335	±0,445	±0,107	±0,443	±0,284	±2,49	±0,320	±0,644	±0,381	±0,281	±0,342	±0,0944	±1,39	±1,39	±1,60	±0,185	±0,860
AVE S16	R28-609	ppm	149.87	79.88	51.79	186.17	21.5	757.77	16.18	157.18	99.86	33.82	179.88	22.18		48.91	148.75	5.03	1093.92
		Stat,Er±(%)	±0,381	±0,455	±0,119	±0,631	±0,312	±2,48	±0,336	±0,749	±0,550	±0,303	±0,432	±0,101		±1,25	±1,75	±0,188	±1,14
AVE S17	Q28-567	ppm	46.04	67.93	29.69	308	29.2	549.12	18.61	167.41	79.76	51.1	63.21	22.68	28.5	35.81	165.37	3.19	731.06
		Stat,Er±(%)	±0,356	±0,449	±0,116	±0,654	±0,311	±2,45	±0,334	±0,742	±0,526	±0,311	±0,333	±0,101	±1,48	±1,24	±1,88	±0,186	±1,05
AVE S18	R28-570	ppm	39.13	99.12	24.63	143.69	23.42	995.71	8.55	52.45	30.23	25.5	26.62	16.12		19.1	114	5.58	309.94
		Stat,Er±(%)	±0,348	±0,443	±0,118	±0,554	±0,319	±2,48	±0,342	±0,638	±0,453	±0,276	±0,278	±0,0965	±1,42	±1,33	±1,46	±0,185	±0,828
AVE S19	R27-507	ppm	110.11	70.49	38.14	294.81	29.07	836.67	22.27	99.7	29.3	38.57	48.96	22.01	17.81	26.84	137.03	3.92	273.75
		Stat,Er±(%)	±0,387	±0,473	±0,123	±0,680	±0,327	±2,51	±0,352	±0,717	±0,464	±0,306	±0,331	±0,105	±1,46	±1,30	±1,82	±0,196	±0,913
AVE S20	P28-526	ppm	27.36	67.3	17.69	209.33	21.31	696.16	11.92	102.2	31.84	31.78	35.62	20.08	8.06	16.24	127.33	3.33	256.12
		Stat,Er±(%)	±0,337	±0,449	±0,107	±0,444	±0,284	±2,45	±0,322	±0,664	±0,398	±0,287	±0,333	±0,0961	±1,46	±1,39	±1,62	±0,186	±0,854
AVE S21	Q28-553	ppm	85.38	83.39	21.6	75.51	3.88	787.27	5.82	410.51	105.55	39.41	107.52	18.21	3.33	54.06	189.2	5.34	465.82
		Stat,Er±(%)	±0,367	±0,475	±0,112	±0,443	±0,296	±2,47	±0,338	±0,835	±0,499	±0,307	±0,418	±0,0994	±1,40	±1,48	±1,58	±0,196	±0,974
AVE S22	Q28-606	ppm	160.59	86.74	52.51	198.35	23.66	1015.99	8.12	448.73	387.41	33.23	169.34	23.93	2.22	63.77	134.58	1.71	1276.28
		Stat,Er±(%)	±0,365	±0,433	±0,118	±0,560	±0,311	±2,51	±0,331	±0,862	±0,826	±0,301	±0,415	±0,0997	±1,46	±1,30	±1,76	±0,179	±1,17
AVE S23	R27-510	ppm	64.25	192.58	18.69	241.02	19.1	376.12	12.28	238.11	97.77	41.35	163.39	20.62	5.5	19.82	102.25	1.96	685.31
		Stat,Er±(%)	±0,340	±0,451	±0,115	±0,588	±0,308	±2,34	±0,332	±0,774	±0,466	±0,314	±0,463	±0,100	±1,44	±1,36	±1,76	±0,177	±1,04
AVE S24	R27-581	ppm	64.76	53.99	26.13	152.1	13.58	675	8	78.02	52.82	26.28	75.91	15.9		22.46	92.05	2.29	693.57
		Stat,Er±(%)	±0,338	±0,420	±0,109	±0,584	±0,291	±2,43	±0,312	±0,652	±0,468	±0,276	±0,329	±0,0929		±1,16	±1,56	±0,174	±0,954

AVE S25	P28-578	ppm	17.07	44.87	14.6	211.03	12.68	969.64	0.93	66.56	15.79	22.4	24.5	12.08	9.77	6.37	112.53	3.75	140.63
		Stat,Er±(%)	±0,331	±0,421	±0,109	±0,602	±0,294	±2,48	±0,314	±0,630	±0,412	±0,269	±0,278	±0,0916	±1,42	±1,16	±1,60	±0,176	±0,784
AVE S26	R28-604	ppm	149.15	69.08	33.07	236.53	16.53	624.96	12.26	151.99	66.71	40.01	169.24	23.16		33.76	161.59	2.53	842.44
		Stat,Er±(%)	±0,380	±0,451	±0,117	±0,641	±0,311	±2,44	±0,335	±0,730	±0,513	±0,302	±0,423	±0,101		±1,24	±1,77	±0,187	±1,07
AVE S27	P28-620	ppm	100.53	140.72	25.8	217.88	12.56	765.36	17.29	54.66	37.15	48.95	197.39	16.19	18.04	19.17	53.25	4.71	422.28
		Stat,Er±(%)	±0,373	±0,491	±0,114	±0,472	±0,300	±2,47	±0,342	±0,695	±0,424	±0,318	±0,498	±0,100	±1,47	±1,47	±1,62	±0,197	±0,971
AVE S28	P28-703	ppm	81.01	63.31	23.08	139.06	13.28	783.03	8.81	124.21	53.61	25.49	92.16	14.49		35.69	97.36	1.98	312.34
		Stat,Er±(%)	±0,347	±0,426	±0,110	±0,588	±0,294	±2,46	±0,316	±0,689	±0,467	±0,278	±0,349	±0,0939		±1,18	±1,52	±0,176	±0,883
AVE S29	P28-623	ppm	24.12	74.23	12.13	130.11	14.13	796.11	6.44	62.94	33.29	28.65	35.15	16.45		6.02	76.48	0.88	339.77
		Stat,Er±(%)	±0,330	±0,424	±0,108	±0,581	±0,292	±2,46	±0,312	±0,647	±0,435	±0,274	±0,291	±0,0921		±1,15	±1,56	±0,174	±0,858
AVE S30	Q28-727	ppm	118.38	60.54	22	97.95	0.02	1078.92	3.36	56.64	32.12	38.4	115.56	17.82	7.96	28.38	91.51	2.6	724.33
		Stat,Er±(%)	±0,367	±0,468	±0,112	±0,444	±0,297	±2,47	±0,337	±0,650	±0,395	±0,291	±0,396	±0,0961	±1,42	±1,46	±1,45	±0,195	±0,942
AVE S31	Q28-726	ppm	104.78	58.16	22.19	93.42	12.14	675.83	9.49	59.75	27.2	32.45	102.26	13.73	4.28	40.31	60.71	3.72	661.62
		Stat,Er±(%)	±0,345	±0,416	±0,108	±0,565	±0,288	±2,45	±0,310	±0,636	±0,425	±0,276	±0,349	±0,0911	±1,45	±1,16	±1,43	±0,173	±0,938
AVE S32	Q28-713	ppm	53.65	50.6	24.45	165.57	17.34	647.64	8.14	72.07	37.06	39.91	61.53	16.46		14.15	97.31		548.71
		Stat,Er±(%)	±0,340	±0,423	±0,110	±0,592	±0,294	±2,45	±0,316	±0,647	±0,441	±0,287	±0,320	±0,0940		±1,17	±1,56		±0,919
AVE S33	R28-850	ppm	56.38	53.7	21.26	183.04	11.92	1703.84	4.63	122.63	138.78	28.97	105.84	14.08	16.2	31.26	69.02	4.42	964.94
		Stat,Er±(%)	±0,336	±0,436	±0,105	±0,431	±0,278	±2,60	±0,313	±0,687	±0,498	±0,284	±0,397	±0,0922	±1,47	±1,36	±1,57	±0,182	±1,04
AVE S34	P28-806	ppm	30.08	70.06	18.57	238.72	28.08	1020.44	10.79	100.1	38.09	31.58	43.51	20.17	6.73	10.81	100.35	2.67	201.52
		Stat,Er±(%)	±0,350	±0,445	±0,119	±0,578	±0,323	±2,50	±0,345	±0,683	±0,480	±0,292	±0,303	±0,101	±1,46	±1,33	±1,65	±0,186	±0,856
AVE S35	Q28-877	ppm	30.4	70.45	12.89	136.43	9.24	771.38	6.74	80.4	49.18	35.54	43.5	18.46	5.44	19.55	100.22		1042.9
		Stat,Er±(%)	±0,343	±0,457	±0,108	±0,440	±0,288	±2,45	±0,326	±0,668	±0,418	±0,293	±0,344	±0,0959	±1,44	±1,41	±1,61		±1,07
AVE S36	R28-825	ppm	82.71	116.28	19.59	128	7.27	657.06	7.24	47.14	20.49	27.15	88.53	15.52	17.21	37.07	61.84	3.8	373.3
		Stat,Er±(%)	±0,345	±0,454	±0,106	±0,427	±0,280	±2,44	±0,317	±0,637	±0,378	±0,280	±0,383	±0,0927		±1,38	±1,45	±0,184	±0,879
AVE S37	P28-780	ppm	25.03	95.28	11.41	124.38	12.55	931.83		70.93	24.84	28	58.61	14.44		8.26	72.89	2.86	208.91

		Stat,Er±(%)	±0,332	±0,449	±0,105	±0,426	±0,280	±2,49		±0,642	±0,377	±0,276	±0,348	±0,0922		±1,37	±1,49	±0,183	±0,806
AVE S38	Q27-156	ppm	45.51	62.23	35.21	281.82	34.12	602.97	19.08	139.99	95.97	46.91	74.51	27.16	13.27	63.85	159.53	1.32	508.85
		Stat,Er±(%)	±0,360	±0,473	±0,114	±0,479	±0,301	±2,45	±0,341	±0,756	±0,495	±0,319	±0,394	±0,103	±1,43	±1,49	±1,90	±0,196	±1,04
AVE S39	P27-161	ppm	73.82	160.13	27.64	126.08	18.85	758.38	13.89	74.61	44.69	30.79	75.7	21.02		31.08	71.18	6.23	460.43
		Stat,Er±(%)	±0,378	±0,509	±0,117	±0,470	±0,310	±2,50	±0,353	±0,697	±0,435	±0,304	±0,396	±0,103		±1,53	±1,54	±0,204	±0,957
AVE S40	P27-106	ppm	99.31	116.28	29.03	185.44	14.3	849.49	5.83	71.5	32.21	30.07	278.51	18.94	17.69	22.22	84.54	1.21	1198.26
		Stat,Er±(%)	±0,377	±0,470	±0,119	±0,642	±0,317	±2,49	±0,341	±0,700	±0,476	±0,298	±0,496	±0,101	±1,48	±1,27	±1,61	±0,190	±1,15
AVE S41	P27-201	ppm	68.94	187.85	21.13	192.84	18.37	1130.23	15.44	60.4	33.5	40.16	84.1	20.79		35.01	120.83	2.38	285.27
		Stat,Er±(%)	±0,368	±0,502	±0,114	±0,471	±0,302	±2,52	±0,344	±0,707	±0,426	±0,307	±0,399	±0,101		±1,49	±1,71	±0,198	±0,947
AVE S42	R27-207	ppm	37.67	56.99	28.17	249.06	20.75	482.51	14.56	109.22	48.92	39.18	62.91	23.52		37.63	110.88	0.53	428.2
		Stat,Er±(%)	±0,352	±0,463	±0,112	±0,466	±0,295	±2,42	±0,334	±0,714	±0,438	±0,303	±0,371	±0,100		±1,45	±1,77	±0,192	±0,967

Annex. 5. Physical property data for each ceramic sample.

Sample No.	Sample Arc. Ref.	Fabric	Apparent density	Real density	Solid density	Total porosity	Open porosity to water	Open porosity to helium	Closed porosity to helium	Weight imbibition coefficient	Saturation index
			ρ_B	ρ_R	ρ_S	ΦT	ΦH_2O	ΦHe	ΦcHe	IC_w	IS
			(g/cm3)	(g/cm3)	(g/cm3)	(%)	(%)	(%)	(%)	(%)	(%)
AVE_S1	P28-211	1	1.90	2.63	2.75	32.20	24.74	27.76	4.44	12.98	88.87
AVE_S2	P28-166	2	1.81	2.71	2.75	34.94	29.88	33.14	1.80	16.47	89.92
AVE_S3	R27-90	2	1.81	2.61	2.70	34.11	28.68	30.57	3.54	15.80	93.56
AVE_S4	R27-87	3	1.94	2.63	2.67	27.87	22.00	26.27	1.60	11.32	83.53
AVE_S5	R28-528	4	1.81	2.78	2.91	39.46	30.53	34.75	4.71	16.78	87.63
AVE_S6	R28-512	3	1.84	2.61	2.69	32.49	28.19	29.55	2.94	15.29	95.14
AVE_S7	R27-465	2	1.83	2.73	2.73	32.85	25.75	32.82	0.02	14.02	78.24
AVE_S8	P28-168	1	1.98	2.70	2.76	28.89	22.14	26.94	1.96	11.17	81.95
AVE_S9	R27-462	2	1.83	2.83	2.83	35.42	31.32	35.30	0.12	17.07	88.48
AVE_S10	R27-478	1	2.06	2.72	2.73	24.80	20.59	24.32	0.49	9.99	84.46
AVE_S11	R27-463	2	1.78	2.72	2.84	38.85	33.27	34.48	4.36	18.59	96.21
AVE_S12	R27-601	2	1.86	2.73	2.77	33.25	28.59	31.90	1.36	15.33	89.38
AVE_S13	R28-540	3	1.94	2.73	2.83	32.72	22.79	29.12	3.60	11.73	78.06
AVE_S14	P27-604	2	1.95	2.75	2.79	30.63	25.58	29.26	1.37	13.09	87.18
AVE_S15	Q28-579	1	2.11	2.71	2.75	23.71	16.71	22.11	1.59	7.90	75.38
AVE_S16	R28-609	2	1.84	2.80	2.84	35.90	30.36	34.16	1.74	16.45	88.65
AVE_S17	Q28-567	3	1.88	2.59	2.70	31.75	24.14	27.52	4.23	12.83	87.49
AVE_S18	R28-570	1	2.07	2.71	2.71	23.72	21.00	23.64	0.09	10.12	88.62
AVE_S19	R27-507	4	1.97	2.55	2.56	23.24	20.10	22.72	0.52	10.18	88.20
AVE_S20	P28-526	1	2.06	2.58	2.75	26.63	18.89	20.02	6.61	9.13	94.08
AVE_S21	Q28-553	4	1.78	2.67	2.73	35.41	31.12	33.25	2.16	17.41	93.36
AVE_S22	Q28-606	2	1.39	2.29	2.34	41.48	39.09	39.16	2.31	27.96	99.55
AVE_S23	R27-510	2	1.77	2.64	2.77	37.85	29.32	33.08	4.77	16.55	88.41
AVE_S24	R27-581	1	2.02	2.77	2.80	28.21	21.61	27.14	1.07	10.67	79.43
AVE_S25	P28-578	1	2.11	2.66	2.66	21.01	16.78	20.72	0.28	7.94	80.76
AVE_S26	R28-604	4	1.81	2.73	2.77	35.21	31.25	33.86	1.35	17.25	92.02
AVE_S27	P28-620	4	1.93	2.58	2.61	26.27	21.42	25.15	1.12	11.06	84.96
AVE_S28	P28-703	1	2.05	2.73	2.79	27.06	21.18	24.79	2.28	10.29	85.22
AVE_S29	P28-623	1	2.15	2.53	2.60	17.98	13.24	14.91	3.06	6.14	88.56
AVE_S30	Q28-727	1	2.04	2.70	2.75	26.45	21.96	24.50	1.95	10.78	89.64
AVE_S31	Q28-726	1	1.96	2.78	2.84	31.37	22.80	29.51	1.87	11.59	77.07
AVE_S32	Q28-713	1	2.10	2.66	2.69	22.43	18.66	21.20	1.23	8.88	87.78
AVE_S33	R28-850	1	2.11	2.72	2.73	23.01	19.39	22.48	0.53	9.18	86.03
AVE_S34	P28-806	1	2.09	2.70	2.72	23.29	16.74	22.50	0.79	7.98	74.21
AVE_S35	Q28-877	3	2.05	2.60	2.62	21.82	19.96	21.04	0.78	9.70	94.64
AVE_S36	R28-825	1	2.07	2.78	2.83	27.40	20.66	25.64	1.76	9.97	80.36

Sample No.	Sample Arc. Ref.	Fabric	Apparent density	Real density	Solid density	Total porosity	Open porosity to water	Open porosity to helium	Closed porosity to helium	Weight imbibition coefficient	Saturation index
			ρ_B	ρ_R	ρ_S	ΦT	ΦH_2O	ΦHe	ΦcHe	IC_w	IS
			(g/cm3)	(g/cm3)	(g/cm3)	(%)	(%)	(%)	(%)	(%)	(%)
AVE_S37	Q28-780	1	2.18	2.54	2.67	19.05	12.69	14.07	4.98	5.80	90.00
AVE_S38	P27-156	3	1.95	2.62	2.70	28.82	22.44	25.59	3.23	11.50	87.45
AVE_S39	P27-161	4	1.93	2.58	2.67	28.69	20.40	25.18	3.51	10.54	80.81
AVE_S40	Q27-201	4	1.83	2.72	2.73	32.81	29.23	32.61	0.20	15.89	89.40
AVE_S41	P27-106	4	1.95	2.53	2.66	28.48	21.01	22.98	5.50	10.77	91.18
AVE_S42	R27-207	3	1.61	2.64	2.67	40.11	25.73	39.17	0.94	15.94	65.49